ps/svw

LEP Note 437
4.2.1983

BEAM ORBIT MEASUREMENT FOR CORRECTION IN LEP

J. Borer, R. Bossart, B. Bouchet, J. Bosser, L. Burnod, D. Cocq,
T. D'Amico, J. Genest, G. Guignard, A. Hofmann and C. Paillard

Contents

4.2.83

Introduction

This note describes the present thinking about the system which measures the first turn trajectory, the equilibrium orbit and the dispersion and beta functions in the LEP lattice. It also gives the general lay-out of the orbit correction system. However, its hardware, such as the correction magnets with their power supplies, is described elsewhere. Furthermore this presentation considers the LEP lattice only; special measurement devices used in the vicinity of the interaction point will be dealt with elsewhere.

1. Relevant parameters and operation modes of LEP

1.1 Injection

In Phase 1 LEP will operate with four bunches per beam with the nominal intensities[1,2)]

$I = 3.0$ mA, $N = 1.67 \cdot 10^{12}$ particles per beam
$I_b = 0.75$ mA, $N_b = 4.17 \cdot 10^{11}$ particles per bunch

These intensities will be accumulated by at least 47 SPS cycles as shown in Fig. 1.1.

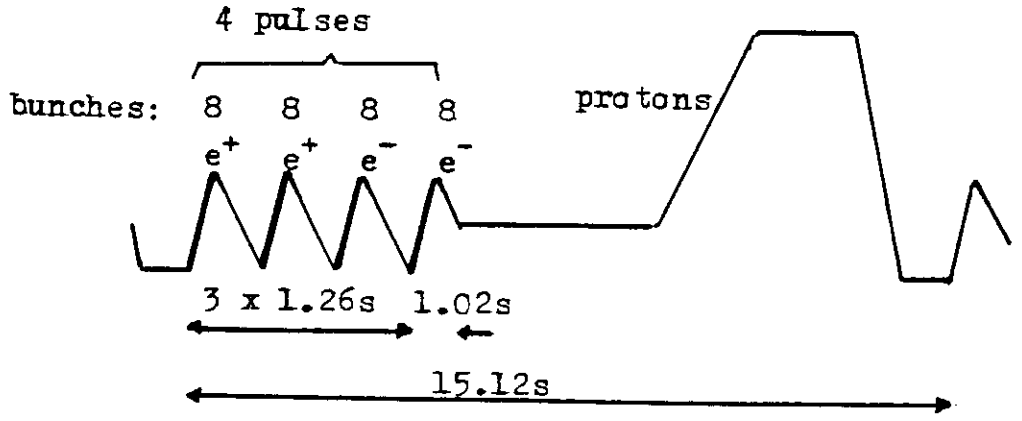

Fig. 1.1 SPS cycle for LEP injection

The intensities injected each cycle are therefore

ΔI/cycle = 63 μA, ΔN/cycle = $3.5 \cdot 10^{10}$ per beam
ΔI_b/cycle = 16 μA, ΔN_b/cycle = $8.6 \cdot 10^{9}$ per bunch

In each such SPS cycle there are two sub-cycles for positrons and two for electrons. Each positron sub-cycle has eight bunches which are injected into the four positron buckets of LEP using a two-turn injection. The intensities injected in single pulse are

ΔI/pulse = 32 μA, ΔN/pulse = $17.6 \cdot 10^{9}$ per beam
ΔI_b/pulse = 4.0 μA, ΔN_b/pulse = $2.2 \cdot 10^{9}$ per bunch

These are the minimum nominal amounts of intensities which are injected into LEP and which should be detected by the beam position monitors. An injection efficiency of 30% had been assumed in deriving the above numbers.

During the initial running-in of LEP the trajectory has to be measured on the first turn. In this case on-axis injection could be used for which the assumed injection efficiency is rather pessimistic. We can therefore regard the above intensity of 4.0 μA/bunch as the minimum current for which the orbit has to be measured. The accuracy with which this first turn orbit should be measured is of the order of 3 mm rms. This gives a minimum value of the measurable product of intensity times displacement

$$\Delta x \cdot I \geq 1.2 \cdot 10^{-8} \text{ A} \cdot \text{m}.$$

With a maximum current of 3 mA/beam to be reached in Phase 1, the dynamic range imposed on the beam monitors covers a factor of about 200.

Once the first turn trajectory is corrected and a reasonable lifetime achieved the equilibrium orbit can be measured by averaging the position measurement over several turns. This should give a more accurate measurement and a better orbit correction.

During the accumulation mode the bunches of the same electron or positron sub-cycle are injected into LEP over several revolutions and injection into the same LEP bucket are spaced by at least 80 ms. Once enough current is accumulated a better measurement and correction of the equilibrium orbit will be possible.

1.2 Bunch numerology

The harmonic number of the LEP RF system is[1] $h = 31320 = 2^3 \cdot 3^3 \cdot 5 \cdot 29$ which gives, with the circumference of $C_{LEP} = 26658.88$ m, an RF frequency of $f_{RF} = 352.21$ MHz.

The SPS has a harmonic number of $h_{SPS} = 4620 = 2^2 \cdot 3 \cdot 5 \cdot 7 \cdot 11$, the circumference is $C_{SPS} = 6911.5\ m = {}^{7}/_{29}\ C_{LEP}$ and the RF frequency $f_{RF}(SPS) = 200.4\ MHz = {}^{33}/_{58}\ f_{RF}(LEP)$.

For nominal operation LEP will have four equidistant electron bunches and four equidistant positron bunches. The closed orbit measurement and correction system will be optimized for this operation mode.

Since the revolution frequency is $f_0 = 11.246$ kHz the bunch frequency for one beam only is $f_b = 44.984$ kHz and the bunch spacing $\tau_b = 22.23\ \mu s$. With both beams circulating the bunch spacing is maximal in the centre of the arc $\tau_{2b} = 11.12\ \mu s$ and gets smaller the closer to the interaction point the observation is made. At the last bending magnet it is $\tau_{2b} = 1.66\ \mu s$.

In some cases, such as the running-in period, LEP might oeprate with fewer bunches per beam and also with one beam only.

If the beam-beam effect is worse than estimated or if the desired bunch current cannot be reached an operation with eight bunches per beam could regain part of the lost luminosity[3,4,5]. In order to make this possible separators have to be installed in the centre of the arc which involves some changes in the dipole magnets to provide the necessary space.

Collisions between electrons from LEP and protons from the SPS have been considered for the far future. For dedicated e-p operation a considerably larger bunch number (e.g. 540) may be used in LEP.

1.3 Bunch length and bunch spectrum

Neglecting the fields induced by the beam in its surroundings the bunch has its natural Gaussian form determined by quantum excitation. The instantaneous current $I(t)$ seen by a pick-up station due to the single traversal of such a bunch is therefore

$$I(t) = I_p e^{-\frac{(ct)^2}{2\sigma^2}} = I_0 \frac{\sqrt{2\pi}\, R}{k_b\, \sigma} e^{-\frac{(ct)^2}{2\sigma^2}} \qquad (1.1)$$

with σ = rms bunch length (in metres), I_p = peak current, R = average machine radius and I_0 = average current of k_b bunches (Fig. 1.2).

The spectrum $\tilde{I}(f)$ of this current seen in a single passage is also Gaussian

$$\tilde{I}(f) = \int_{-\infty}^{+\infty} I(t) e^{-j\omega t}\, dt = \frac{I_0}{k_b f_{rev}} e^{\frac{-(2\pi f)^2\sigma^2}{2c^2}} \qquad (1.2)$$

where f_{rev} = 11.25 kHz is the revolution frequency. The rms frequency of this spectrum is

$$f_s = \frac{c}{2\pi\sigma}$$

which is listed in Table 1.1. Note that the spectrum contains positive and negative frequencies and that the Fourier transformation is normalized in such a way that $\tilde{I}(f)$ is given in A/Hz.

In LEP each beam has k_b = 4 equidistant bunches. The spectrum of a single beam with bunches of equal intensities consists of lines spaced by $4 \cdot f_{rev}$. (Fig. 1.2).

$$I_{kb}(t) = I_o \sum_{p=-\infty}^{\infty} \exp -\frac{1}{2} \frac{p k_b 2\pi f_{rev} \sigma}{c} \qquad (1.3)$$

The line spectrum of the two counter-rotating beams is more complicated and depends on the location of the beam observation. This is due to the fact that the time spacing between the passage of the e^+ and e^- bunches is different at different monitor locations.

The monitors themselves have a broad-band response and cannot resolve the line structure of the spectrum. Only the single traversal spectrum (1.2) has therefore to be considered for monitor response calculation. However the time spacing of the bunches is important for all considerations involving measurements of individual bunches and beams.

For large intensities the fields induced by the bunch itself will alter its form, an effect which is usually called bunch lengthening (or shortening). The bunch form is no longer Gaussian under these conditions but one often makes a Gaussian fit through the little-known actual bunch form.

In Table I the rms bunch length σ, the peak current I_p and the rms frequency $\omega_{rms}/2\pi$ of the bunch spectrum are listed for different conditions. At the low injection intensity self-fields are negligible and the natural bunch length can be used. For higher intensities the bunch length has been calculated with tracking programs[6,7,8]

condition	E (GeV)	$\frac{I_0}{k_b}$ (mA)	σ (mm)	I_p (A)	$f_s = \frac{c}{2\pi\sigma}$ (GHz)
one injection pulse	20	0.004	16	2.7	3.0
nominal current for acceleration	20	0.75	19	427	2.5
nominal current	50	0.75	12	670	4.0

Table 1. Bunch length, peak current and bunch spectrum for different conditions.

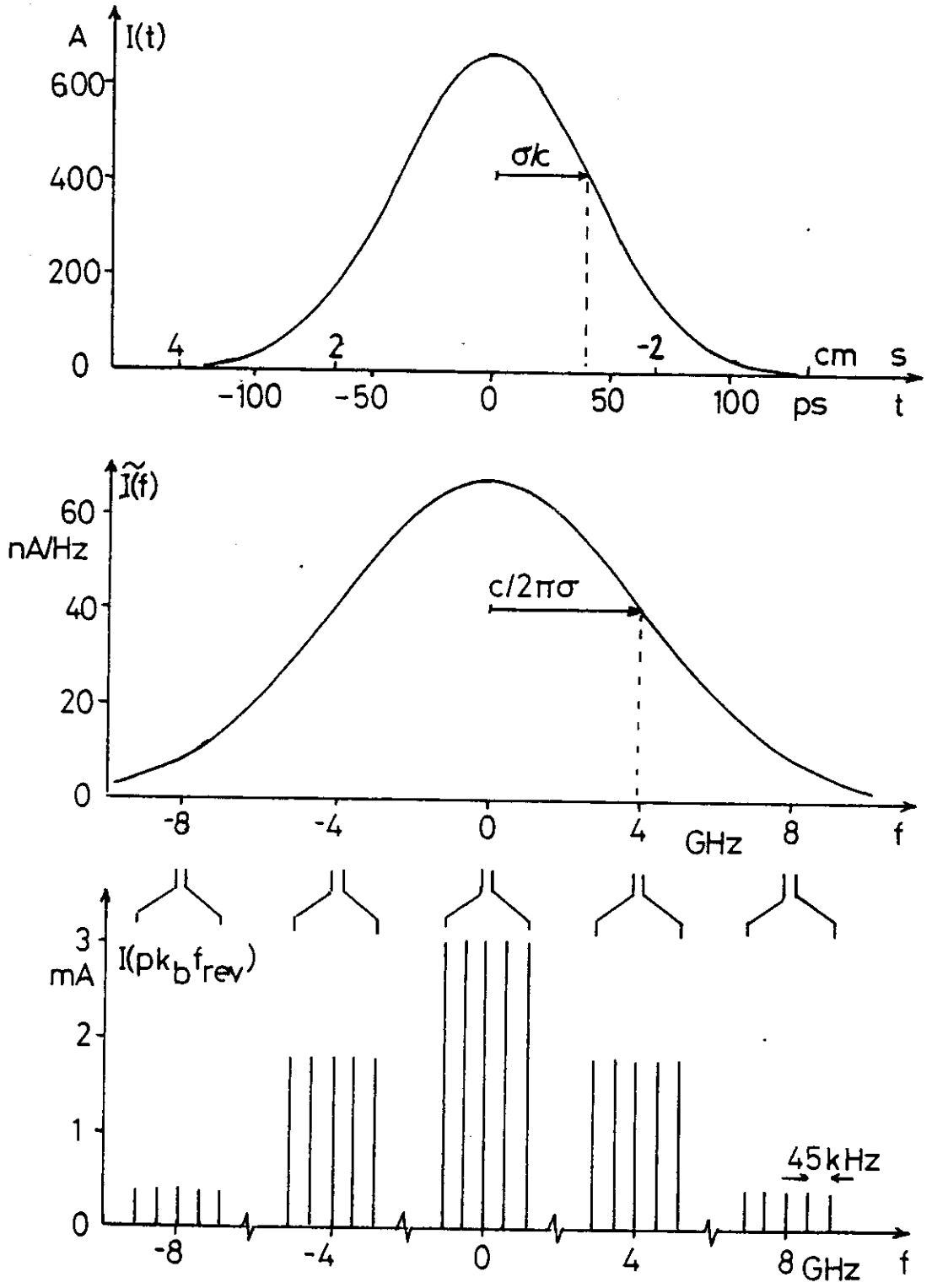

Fig. 1.2. Time-dependent current I(t), single traversal current spectrum $\tilde{I}(f)$ and multiple traversal line spectrum $I(p\ k_b f_{rev})$ of four equal Gaussian bunches having a total current of 3 mA and a length of σ = 12 mm.

1.4 Electron and positron orbits

In LEP the energy loss per revolution due to synchrotron radiation is 223 MeV at 51.5 GeV. With only two RF stations being installed of Phase 1 the beam just leaving an RF system will have an excess of relative energy of $1.08 \cdot 10^{-3}$ while the other beam has a lack of energy of the same amount. This leads to a horizontal separation of the two beams which is maximal at the end of the arc. There at the maximum dispersion of D = 2.22 m this separation is about 4.5 mm. In the presence of field errors also the vertical orbits of the two beams could become different[9,10]. As a consequence of these effects the beams could be displaced relative to each other at the interaction point and the luminosity reduced.

It is therefore desirable that the orbit of one beam can be measured in the presence of the other at least for the nominal operation with four bunches per beam. Furthermore these effects have to be taken into account when the orbits are corrected.

1.5 Energy ramping

In Phase 1 the energy per beam could go from a minimum of about 18 GeV to a maximum of about 77 GeV. It is planned that the energy will be ramped linearly with a speed of about 1 GeV/s after injection is completed. the total ramping time is therefore of the order of a minute. The closed orbit has to be controlled during this process which can probably be done using fixed correction files. It might, however, be necessary to measure the orbit several times during ramping. Furthermore the betatron and synchrotron frequencies have to be controlled.

2. Distribution of monitors and correctors

The proposed distribution of monitors and correctors is compatible with the two considered phase advances of 60° and 90° per cell and with the use of local bumps for orbit corrections. It is the result of PETROS[11] and PETROC[12] calculations[13,14,15] where the effects of alignment and excitation errors of the magnetic elements on the orbit are evaluated and subsequent corrections simulated.

A position monitor is installed at each quadrupole. Most of them read only the beam displacement in the focusing direction of the adjacent quadrupole. Only a few monitors in the interaction regions read horizontal and vertical beam positions. The correctors are small independent magnets[16]. They are distributed in such a way that two out of three lattice quadrupoles have a corrector in their vicinity, acting always in the focusing direction of the quadrupole. Again a somewhat denser distribution is used in the interaction region. With this lay-out localized correction bumps can be made spanning 180° in the 60° lattice and with a span of 180° or 360° in the 90° lattice. The distribution of monitors and correctors and the local bumps are shown in Fig. 2.1. Minor changes of the monitor and corrector positions around the interaction may be necessary when the other equipment to be installed there is finalized.

With this distribution and using a minimization around the interaction region and localized bumps elsewhere for correction PETROC calculations have been carried out[15]. The main results are shown in Table 2.1. The residual errors of the corrected orbits are first given without taking the error of the orbit measurement into account. This measurement error is due to alignment error of the monitor and due to read-out errors. The rms alignment error between the electrical centre of the monitor and the magnetic centre of the quadrdupole is estimated to be of the order of 0.2 mm using typical individual alignment errors of 0.1 mm rms. The rms read-out error after calibration may be of the order of 0.2 mm. The measurement of the beam position with respect to the quadrupole axis has therefore an rms error of about 0.3 mm rms. External noise entering into the read-out system could increase this error further. We assume here a total rms measurement error of about 0.5 mm to get the final residual orbit distortions listed in Table 2.1. As can be seen from these numbers the orbit corrections are quite efficient for both phase advances.

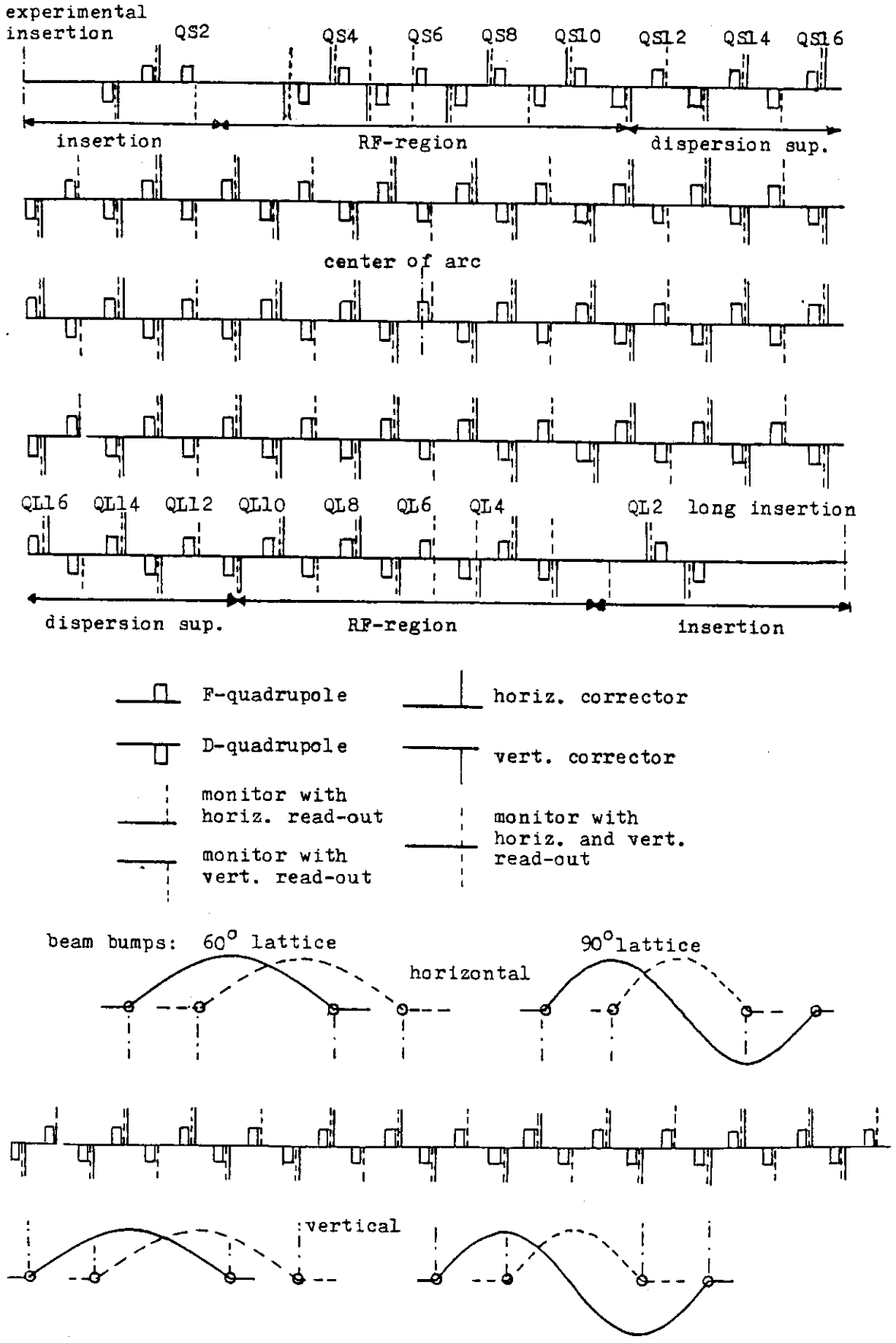

Fig. 2.1 Distribution of position monitors and orbit correctors over one octant and possible local correction bumps.

phase advance per cell		deg.	60°	90°
dipole errors:	horiz. alignment	mm	0.12	0.12
	tilt	mrad	0.24	0.24
	excitation	ΔB/B	$2.5 \cdot 10^{-4}$	$3 \cdot 10^{-4}$
quad. errors:	horiz. alignment	mm	0.12	0.12
	vert. alignment	mm	0.12	0.12
	tilt	mrad	0.23	0.23
	excitation	ΔB/B	$5 \cdot 10^{-4}$	$5 \cdot 10^{-4}$
orbit stability:				
number of machines tried			10	54
" " stable machines			10 (100%)	19 (35%)
" " damped "	before correction		2 (20%)	7 (37%)
" " " "	after "		10(100%)	7 (37%)
orbit errors:				
horiz., before correction		mm	6.8	6.6
" , after "		mm	0.4	0.4
" , " "	incl. 0.5 mm reading error	mm	0.64	0.64
horiz. correction factor			0.094	0.097
vert., before correction		mm	11.7	9.2
" , after "		mm	0.5	0.7
" , " "	incl. 0.5 mm reading error	mm	0.71	0.86
vert. correction factor			0.060	0.094
vert. dispersion before correction		mm	598	540
" " after "		mm	146	188
" " correction factor			0.24	0.35

Table 2.1. Results of PETROC calculations for LEP 11 with 60° and 90° phase advance per cell. All errors refer to rms values.

The strength of the orbit corrector has to fulfill three requirements. It has to be sufficient to apply the corrections called for in the PETROC simulations; the kick due to a single quadrupole misaligned by 1 mm should be able to be compensated by the corrector at top energy; local beam bumps will be used to scan the available aperture at injection energy in order to find possible obstacles. The resulting required corrector strengths are listed in Table 2.2. In most cases the third of the three requirements determines the corrector strength. If necessary this requirement could be somewhat reduced by using longer bumps involving four correctors for aperture scanning.

The setting errors of the correctors should be small enough for their contribution to the residual orbit error to be negligible. This gives an error in the correctors' strength of $\sim 2 \cdot 10^{-5}$ Tm.

phase advance per cell	deg.	60°	90°
horiz. correctors in the arc	Tm	0.029	0.026
vert. " " " "	"	0.019	0.019
horiz " " " RF sections	"	0.036	0.035
vert. " " " " "	"	0.031	0.025
horiz. " near QS2, QS4	"	0.050	0.050
vert. " " QS1	"	0.074	0.074

Table 2.2. Required corrector strengths

An additional requirement applies to the setting accuracy of the vertical correctors. To minimize depolarization of the beam certain harmonics of the vertical closed orbit should be corrected to a value which is below the accuracy of the measurement system. It will be done by creating this harmonic with a set of correctors and varying its strength while the polarization is measured[17]. This optimization of the polarization requires small steps in the corrector strength. To estimate this step size it was assumed that the orbit harmonic mentioned is created by using 16 correctors. The setting accuracy of the correctors was then calculated so that the bump corresponding to a step equal to this resolution should not affect the polarization by much more than 1% at 40 GeV[18]. Therefore we also obtain for the step size or accuracy of each corrector about $2 \cdot 10^{-5}$ Tm. About the same value is obtained if the steps used in the polarization optimization at PETRA[17] are scaled to LEP conditions. A setting accuracy of $2 \cdot 10^{-5}$ Tm for the correctors seems to satisfy all requirements. This corresponds to a relative accuracy with respect to the maximum strength of not more than $5 \cdot 10^{-4}$ for most correctors. It should be noted that sometimes the orbit has to be corrected and the polarization optimized while the beam is circulating. Under these conditions the corrections cannot be cycled to avoid hysteresis effects.

3. Beam monitor design and characteristics

3.1 General considerations

The bunch length being about 4 cm (4σ), the probe system does not need to be longer to "sense" practically all the charges of the bunch.

The monitor has to be integrated in the vacuum chamber made of extruded aluminium tubing. Its position should be next to the quadrupoles with an rms alignment tolerance of 0.1 mm relative to the quadrupole references.

Two short straight section (SSS) dispositions have been studied:

version 1 , from the "Blue Book"[19], where the quadrupoles are approximately in the middle of the SSS and the monitors about 70 cm away from the chamber end and bellows assembly (Fig. 3.1);

version 2 , where the quadrupoles are at the end of the SSS and the monitors next to the bellows assembly (Fig. 3.2).

In version 1, the monitor has to be integrated in the quadrupole chamber in order to avoid additional large flanges and the interruption of the chamber water-cooling channels. It should also be repairable in situ which implies the use of demountable flanges for the electrodes.

In version 2, the monitor can become a separate unit, independent of the chamber fabrication processes, but is then next to the bellows system which contains RF contacting elements such as bellows or sliding contacts. This proximity may produce (especially with the sliding contacts) perturbations to the monitor characteristics. These perturbations are being evaluated both theoretically and by model measurements on the test set-up (see Section 3.6).

Since each of these solutions presents advantages, they have both been studied.

In the bending arcs the monitors will be exposed to synchrotron radiation and, in order to avoid direct impact on the horizontal probes and interference with the cooling channel, their assembly has to be skewed. The

vertical and horizontal information can then be obtained by sum and difference between the four probes.

Since the same probes will sense both the electron and positron bunches, it would be an advantage to be able to distinguish the two kinds of signal by their polarity in addition to their timing sequence.

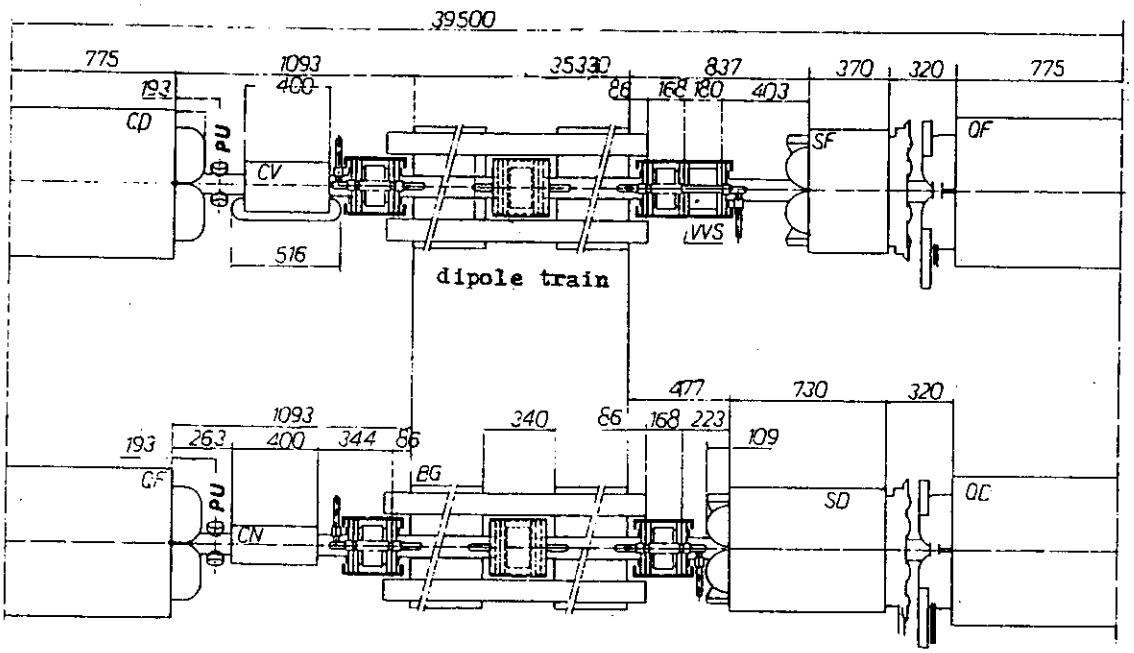

Fig. 3.1 Layout of a short straight section, version 1.

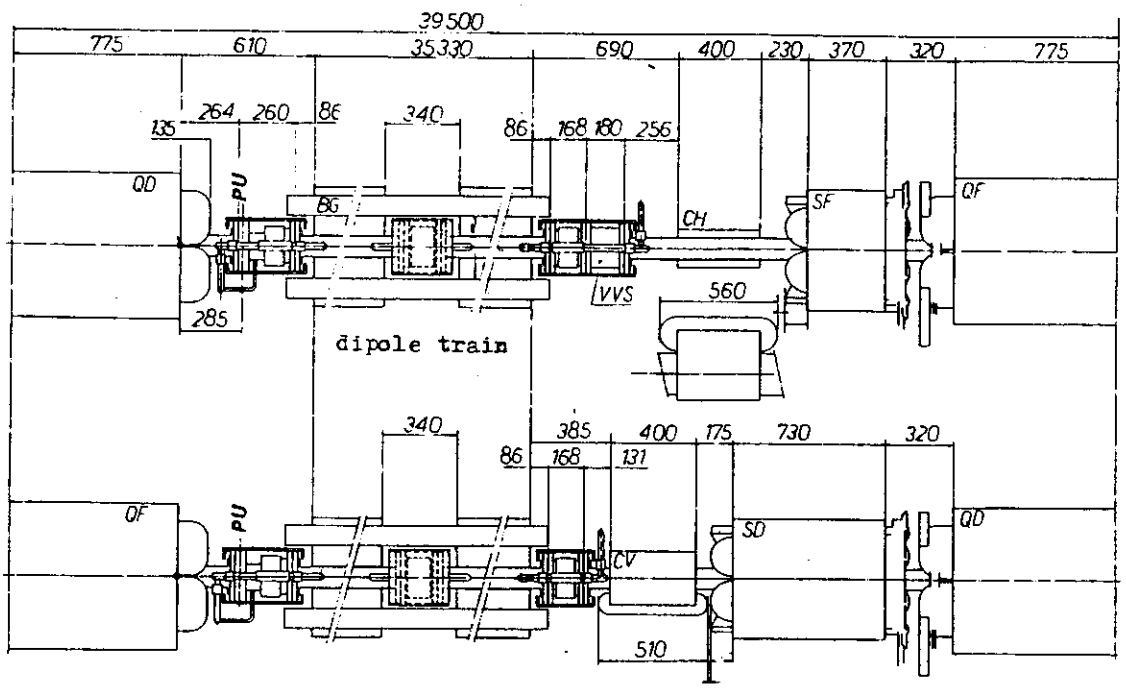

Fig. 3.2 Layout of a short straight section, version 2.

Different types of sensors can be considered:

- probes based on the pure magnetic coupling; they would not present the polarity advantage

- probes based on the electro-magnetic coupling such as the directional couplers[20]; they would present the advantage of electron-positron signals separation, with an isolation between the two outputs of about 40 dB. Their integration into the available space and into the extruded vacuum chamber is more complicated and requires double the number of feedthroughs

- probes based on the pure capacitive coupling such as button electrodes; they present the advantage of signal polarity and simplicity of construction[21]. This type of probe is already used in many electron machines and has been chosen for LEP[21-25].

It results from these general considerations and from the geometry of the chamber that the buttons can have a diameter between 20 and 30 mm and a disposition as represented in Fig. 3.3.

Another very important aspect is the influence of the ionising synchrotron radiation on the materials of the probes, on the electrical signals and on the long-term stability of the monitor characteristics. A study of the radiation levels[26-28] to which the button electrodes will be submitted shows an integrated dose of the order of:

at 51.5 GeV/c : 10^{10} rad per year of operation (3000 h)
at 85 GeV/c : $4 \cdot 10^{10}$

The geometry of the electrode disposition results in a dose which is twice as large for the outer electrodes as for the inner ones[26,27].

Another important aspect is the peak dose rate due to the pulsed nature of the γ radiation. the peak value is very high due to the duty factor of the bunch (bunch length versus LEP circumference). The calculation has resulted in a time function[27] with a leading edge similar that of the bunch current time function, since it is produced by the forward scattered photons

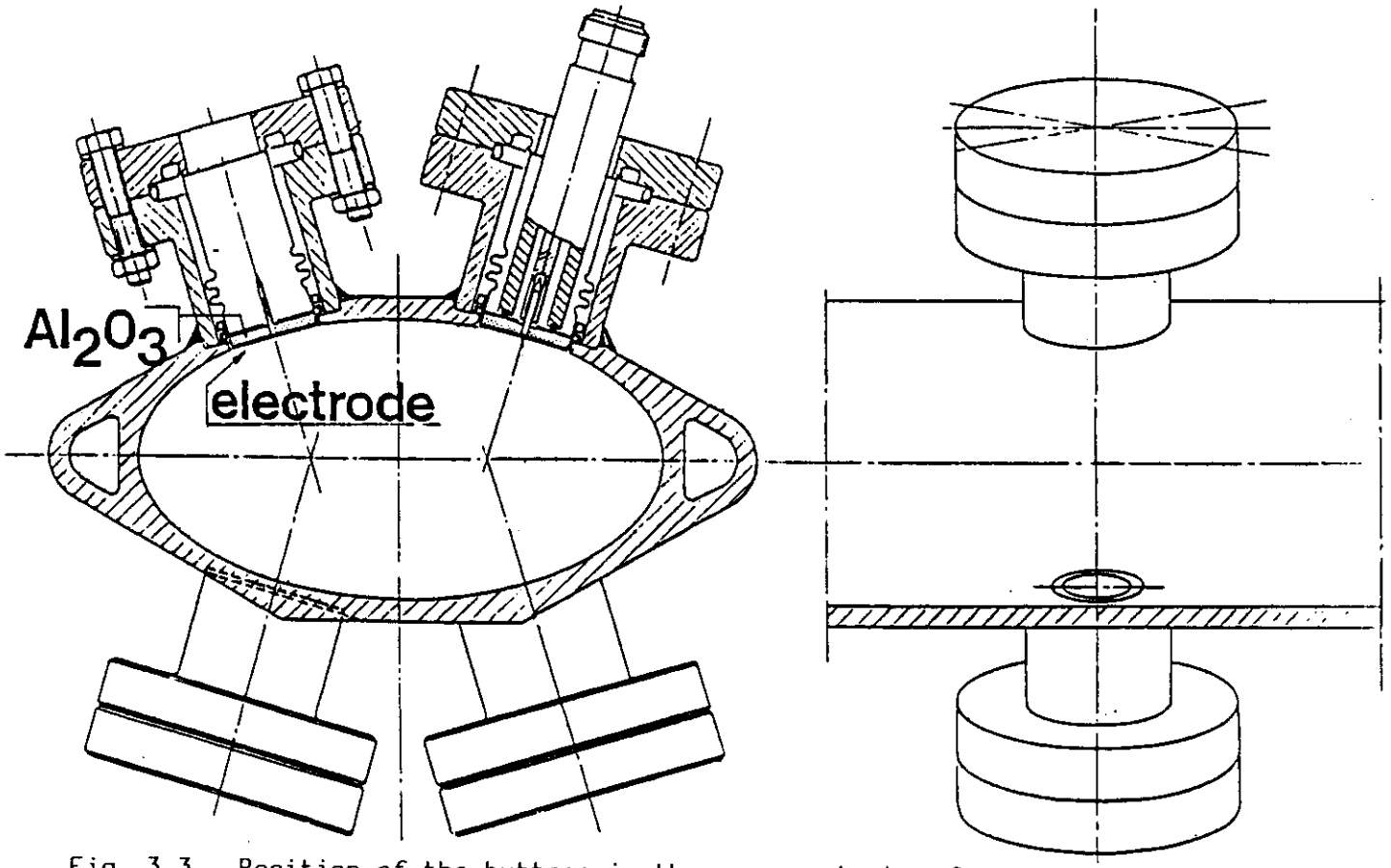

Fig. 3.3 Position of the buttons in the vacuum chamber for version 1.

which have about the same velocity as the bunch. But the trailing edge has a longer time constant since it is produced by the back-scattered photons which have then a longer path to travel. This time function is represented in fig. 3.4 .

The calculated peak dose rate has the following values:

51.5 GeV/c : 1.5 : 10^7 Rad/sec
85 GeV/c : 1.3 : 10^8 Rad/sec

for the outer electrodes.

For such integrated doses and dose rates, very little information is available to predict with precision the ionisation effect on the ceramics needed for the electrode assembly and its vacuum feedthrough.

The stability of the elctrode capacity is important for the monitor performance. It imposes that the dielectric constant of the ceramic should not change with the high photon doses absorbed. Here also very little information was available. It resulted from specialist consultation (Commissariat à l'énergie atomique de Paris) that its purity and metallisation procedure

It was decided to have prototype electrodes (Fig. 3.5) tested with a pulsed γ source (Euphrosyn, 1.4 MV, 40 ns, 10^{10} Rad/s) with peak dose rate in excess of the LEP worst case. In addition an integrated dose test should show on the prototypes if the Al_2O_3 dielectric constant varies with the highest dose possible in future LEP phases (10^{11} Rad/year). These tests done by the CEA[29] gave favourable results and show that no mechanical damage has been produced by the high photon current and that the dielectric constant of Al_2O_3 was not affected by the high radiated dose.

Another critical aspect of the high radiation level is the air ionisation in the coaxial line after the coaxial feedthrough (Fig. 3.3). The pulsed nature of the synchrotron light may produce an ionisation chamber effect and therefore perturb the signal in addition to the secondary electron current produced by photons on the electrode surface and volume[30,31].

Finally, the air ionisation also produces ozone and nitric acid with the ambiant humidity, which may corrode the electrical contact within the connector.

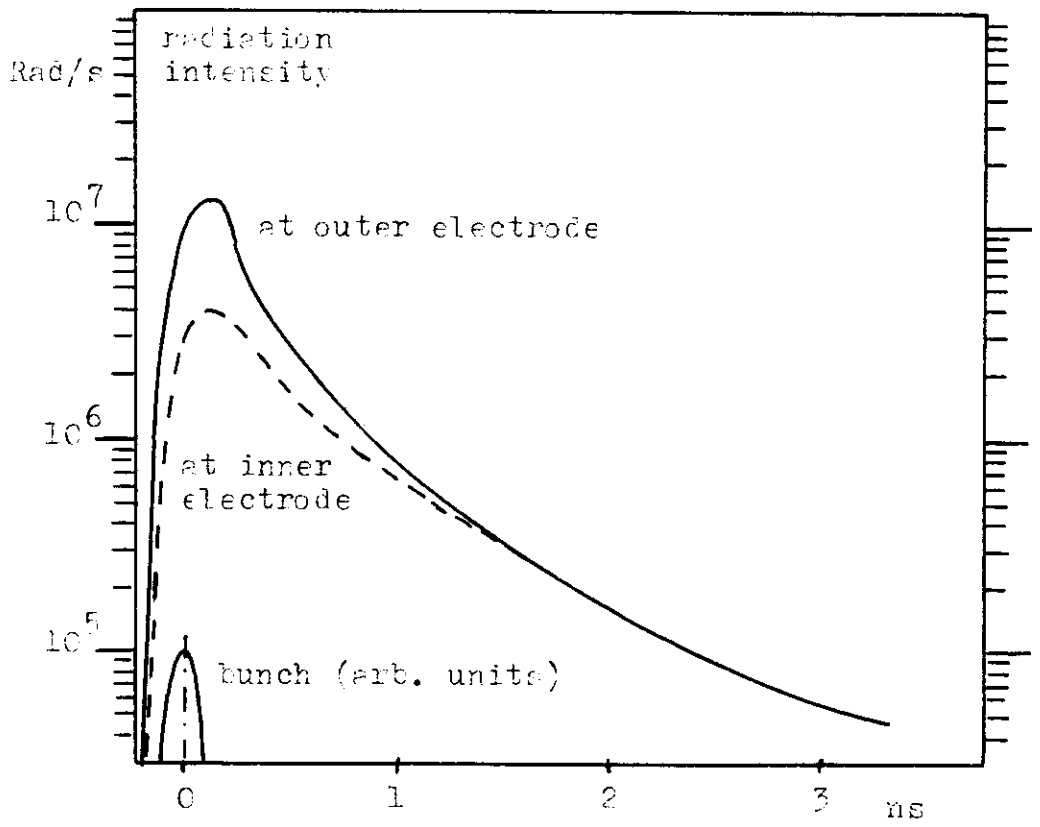

Fig. 3.4 Time dependence of the radiation intensity at the buttons for the passage of a bunch with $N_b = 7.66 \cdot 10^{11}$ particles, $\sigma = 2.25$ cm and $E = 51.5$ GeV[27].

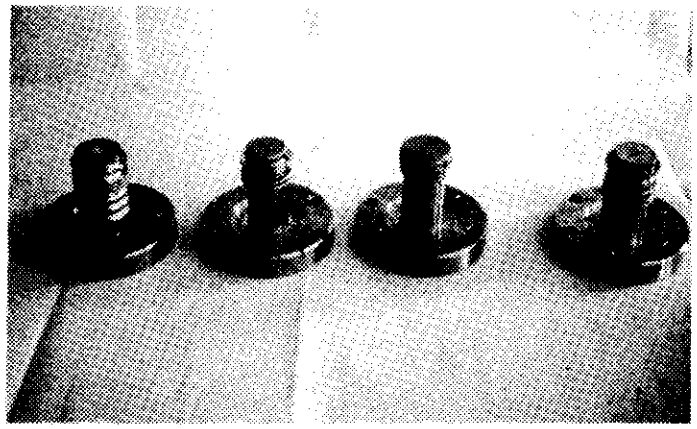

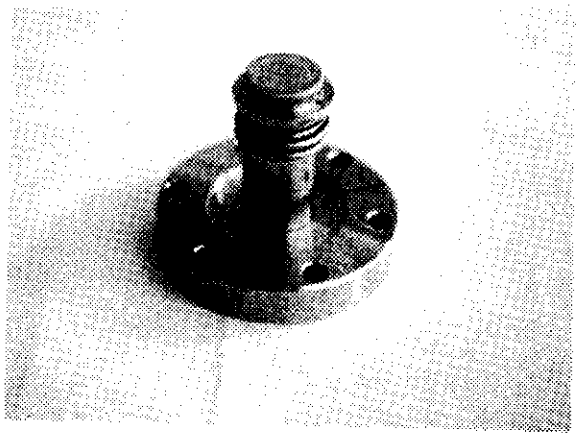

Fig. 3.5 Photos of model electrodes

3.2 Prototype button electrodes for electrical and radiation tests

A first design has been produced prior to having the results of the radiation calculation. It is based on the following concepts:

- the version 1 disposition, whereby the monitor is away from the bellow system, has been chosen. It implies four flanges for the four electrodes;

- the flanges are used for the transition aluminium to stainless-steel[32];

- the electrode mechanical support and the feed-through are combined; this solution allows a mechanically stable and reproducible electrode structure, metallisation on ceramic, and low cost;

- the positioning of the electrode is independent of the flange (bellows).

This type of button electrode is represented in Fig. 3.3. Five manufacturers have produced prototypes based on this design, but with some freedom in the actual realisation.

These prototypes (Fig. 3.5) have been radiation tested, as stated in section 3.1.

The electrical response of the capacitive electrode is described in sections 3.5 and 4.1. Prototypes with metallised electrodes were tested (see section 3.6) in a chamber configuration corresponding to the PU version 1 with its four flanges. They presented a ringing due to the length of line within the 3 mm thickness of the Al_2O_3 disc where the wave velocity is reduced by $\sqrt{\varepsilon_r} \sim 3$ and therefore is equivalent to a perturbing length increased to about 10 mm. Different models were built and the conclusion was that the electrode diameter is surprisingly not critical, the effective distance to ground should be minimum, <1 mm and the connected coaxial line as free of reflexions as possible.

3.3 Beam monitor model 1

A final electrode model has been built taking the preceding test conclusions into account (Fig. 3.6). In addition its electrode disc is made thicker for better shielding of the ceramic against the scattered synchrotron light and the ceramic volume is reduced to a small centring ring.

The feedthrough[25] which supports the central conductor and the electrode is pushed as far as possible away from the radiation source in order to profit from the collimation effect of the outer tube and external lead shield. In this way, the first part of the coaxial line is under vacuum and will not suffer from ionisation problems. The first connector and cable should then not be submitted to too high a level of radiation. The length of this electrode assembly has not yet been optimised.

The mechanical construction of the electrode should be very stable, reproducible and possibly tunable. The next step is to build final prototypes.

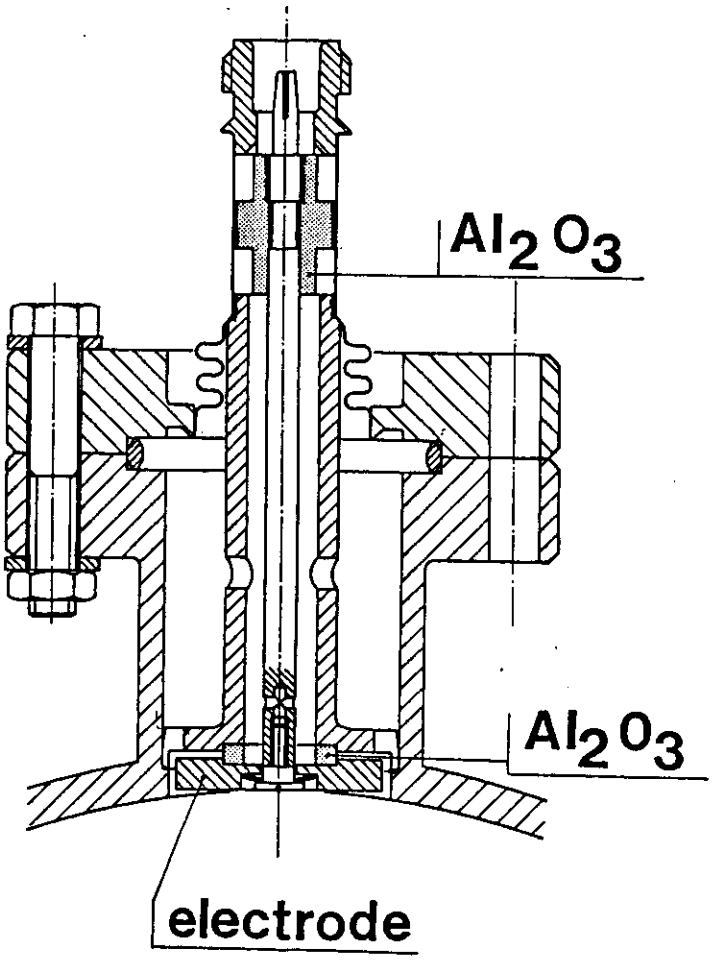

Fig. 3.6 Improved button construction.

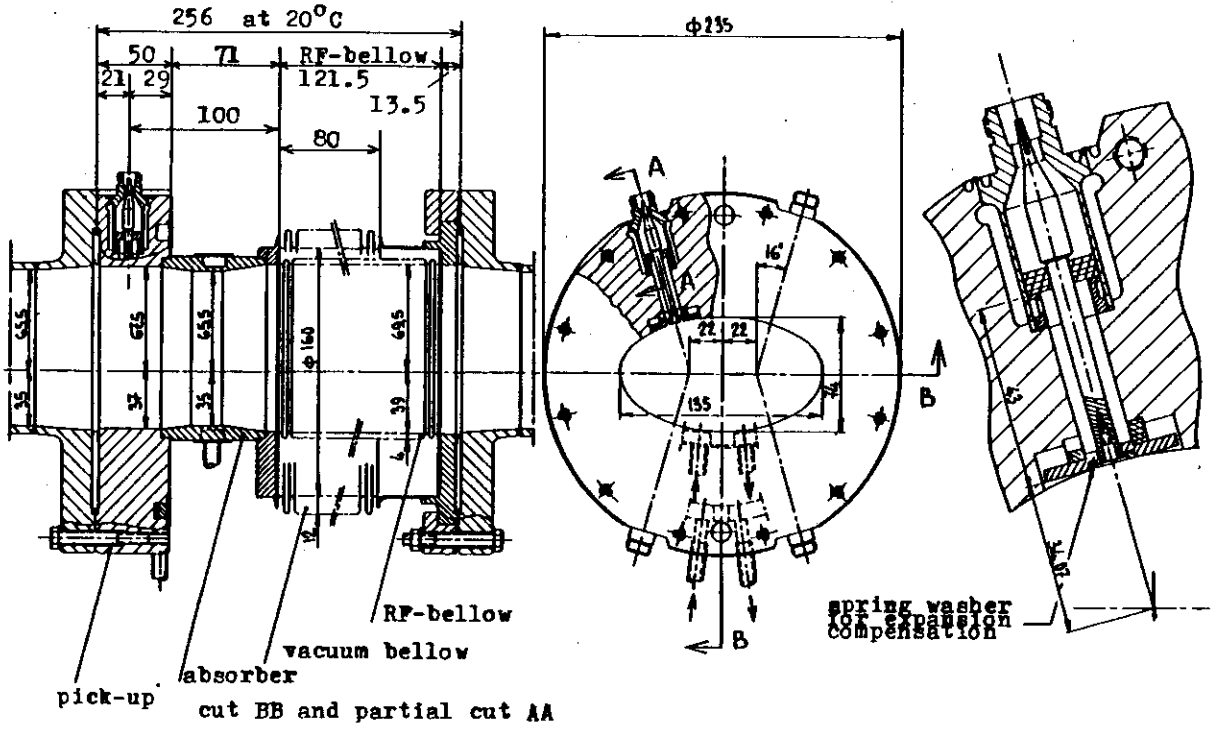

Fig 3.7 Beam position monitor model 2 having the buttons integrated in a flange.

Figs. 3.3 and 3.6 show the beam monitor on a standard quadrupole chamber. It does not interfere with the cooling channels and will house a set of four balanced button electrode assemblies. The monitor chamber should have the following characteristics:

- mechanical tolerances on the geometry of the electrode seats should allow an rms tolerance of 0.1 mm between the electrical and mechanical axis of the monitor after all chamber treatments and lead shield application. This tolerance should be stable in time;

- the monitor support should allow an rms alignment tolerance of 0.1 mm between its mechanical axis and the quadrupole references;

- the beam monitor chamber is a fixed point of the vacuum system and should be rigid enough to support all efforts.

The construction of the monitor chamber is bound to the general vacuum chamber technology. Feasibility studies are on their way, but not yet finished. Electron-beam and friction welding are promising methods for joining the extruded Al-alloy with forged or machined seat preforms. A final machining should give the required precision. A machined monoblock solution is also being studied.

If needed a final electrical test, with reference electrodes, will determine the monitor electrical axis which will be mechanically transferred on the external fixation and reference plate. This version 1 beam monitor allows more isolation from electromagnetic interference due to the bellow assembly. However, it presents drawbacks for its fabrication and installation due to the fact that it is bound to the SSS chamber fabrication processes.

3.4 Beam Monitor Model 2

An alternative solution has been studied whereby the monitor and chamber have different fabrication lines. It uses the same button electrode structure, but the coaxial lines, with feedthrough and connectors, are machined in a disc which could be either stainless steel or Al. Fig. 3.7 shows the model 2 construction. This monitor having a disc form could be sandwiched between the two chamber flanges. However, in order to save one vacuum joint, a welded assembly with its neighbouring bellows has been chosen. This type of

monitor is well adapted to the so-called version 2 disposition (Fig. 3.2) where the quadrupoles are at the end of the SSS. This solution has the advantage of fabrication and calibration as being independent of the vacuum chamber. In addition, it will require cooling for the higher energy level of LEP. Model 2 should ease the fabrication processes to reach the required overall precision. A model of this monitor version has been fabricated and is being used for the measurement of the bellows assembly interferences.

3.5 Electrical characteristics of the beam monitor

3.5.1 Sensitivity to beam current

If one only considers the image charge induced by the beam electrical field, without longitudinal component, the influenced voltage follows the Faraday's law in a pseudo static state, fig. 3.8.

$$V_e(t) = \frac{Q_e(t)}{C_e} \qquad (3.1)$$

with $Q_e(t)$ the instantaneous charge on the button electrode and C_e the capacity of the electrode.

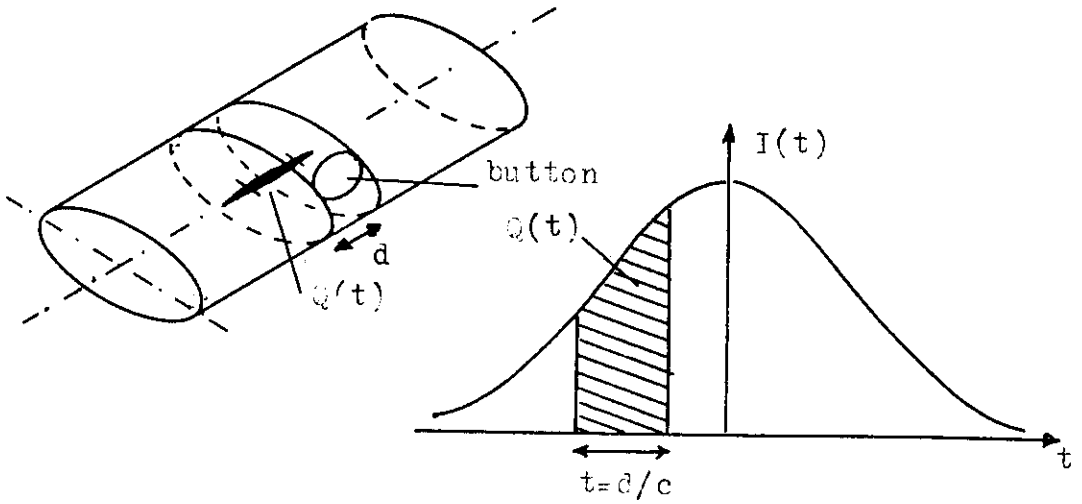

Fig. 3.8 Coupling from beam to electrode.

If one defines Q (t) as the instantaneous beam mean charge over the length d, it allows it to be related to the instantaneous beam current, I(t) knowing that the beam velocity is c :

$$\Delta t = \frac{d}{c} \quad \text{and} \quad Q(t) = \int_{t}^{t+\Delta t} I(t)dt \approx I(t)\,\Delta t \qquad (3.2)$$

$$\text{Hence } Q(t) = I(t)\cdot\frac{d}{c} \qquad (3.3)$$

The relation between the image charges on the electrode $Q_e(t)$ and the total image charges on the cylinder of length d, equal to the beam charges of the same length Q (t), is in our approximation simply the area ratio:

$$\frac{Q_e(t)}{Q(t)} \approx \frac{A_e}{A_{cylinder}} = \frac{\pi d}{4p} \qquad (3.4)$$

with p = perimeter of an ellipse with major and minor half-axes a and b.

It results from equations 3.1 to 3.4 that[33]:

$$V_e(t) = I(t)\,\frac{\pi d^2}{4cC_e p} = I(t)\,Z_\infty \qquad (3.5)$$

which can be expressed as a coupling impedance Z_∞ in the case of unloaded electrode (Fig. 3.9).

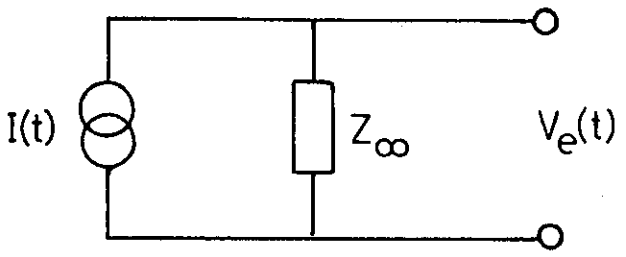

Fig. 3.9 Equivalent circuit for the beam-to-electrode coupling.

Remarks

Such a model is valid:

- for bunch length $\geqslant$ d
- for a simplification whereby the image charges have a constant density on the ellipse perimeter p
- up to frequencies where the P.U. can be considered as pure capacitance[34]. At higher frequencies the response is determined by resonances.

We calculate Z_∞ for the optimized model with the parameters: axes of the ellipse a = 65.5 mm, b = 35 mm, circumference p = 323 mm, electrode diameter d = 26 mm and electrode capacity C_e = 17 pF.

Using (3.5) gives :

$Z_\infty = 0.323\ \Omega.$

Using the correct charge distribution in an elliptic chamber[35] we get:

$Z_\infty = 0.34\ \Omega.$

Measuring Z_∞ by observing both the attenuation of the pulse response and the transfer function gave :

$Z_\infty(\text{measured}) = 0.35\ \Omega.$

Since the final button parameters may be slightly different we take for the time being round numbers :

$$Z_\infty = 0.30\ \Omega,\ C_e = 15\ \text{pF} \qquad (3.6)$$

3.5.2 Sensitivity to the transverse beam position

The transverse response of the monitor is expressed as the ratio between the difference signal Δ and the sum signal Σ. The difference signal for a horizontal monitor (Fig. 3.10) is obtained by forming first the sum of the signals from button 2 and 4 and the sum of buttons 1 and 3 and then taking the difference between these 2 sum signals. Ideally the response signal should be proportional to the horizontal displacement x of the beam; in reality the response is more complicated and can be expressed as:

$$\left(\frac{\Delta}{\Sigma}\right)_x = k(o,o)(1 + g(x,y))x \qquad (3.7)$$

for a horizontal monitor.

Taking as an approximation a monitor in a circular chamber of radius a ≅ 50 mm with buttons at ±45° with respect to the orbit plane, one gets :

$$k(x,y) = \frac{\sqrt{2}}{a} \quad ; \quad g(x,y) \approx -\frac{x^2-3y^2}{a^2} + \frac{x^4-3y^4-2x^2y^2}{a^4} + \ldots\ldots$$

A more accurate calculation gives :

$$g(0.2,0.0) = -3.8\% \quad \text{and} \quad g(0.2,0.2) = 7.3\%$$

With this circular approximation for the LEP chamber with a = 50 mm not introducing the correction factor g(x,y) would result in a proportional error less than 8% for a beam position located inside a circle with 10 mm radius.

The sensitivity near the centre for x = 0.1 mm ($\frac{x}{a} = \frac{0.1}{50} = 0.002$) corresponds to $\left(\frac{\Delta}{\Sigma}\right)_x = 2.8 \cdot 10^{-3}$.

If we take the correct charge distribution in an elliptic chamber[35] we find for the horizontal monitors on the medium plane y = 0

$$\left(\frac{\Delta}{\Sigma}\right)_x \approx 0.041\ (1-0.00071x^2)x \qquad (3.8)$$

where x is the horizontal beam displacement in mm. This value agrees well with that measured for the version 2 prototype (Fig. 3.11).

The non-linearity of the monitor response (3.8) is only important for large deviations from the centre and does not affect the orbit correction much if it is done in several iterations. However it has to be taken into account if a large orbit distortion has to be measured accurately.

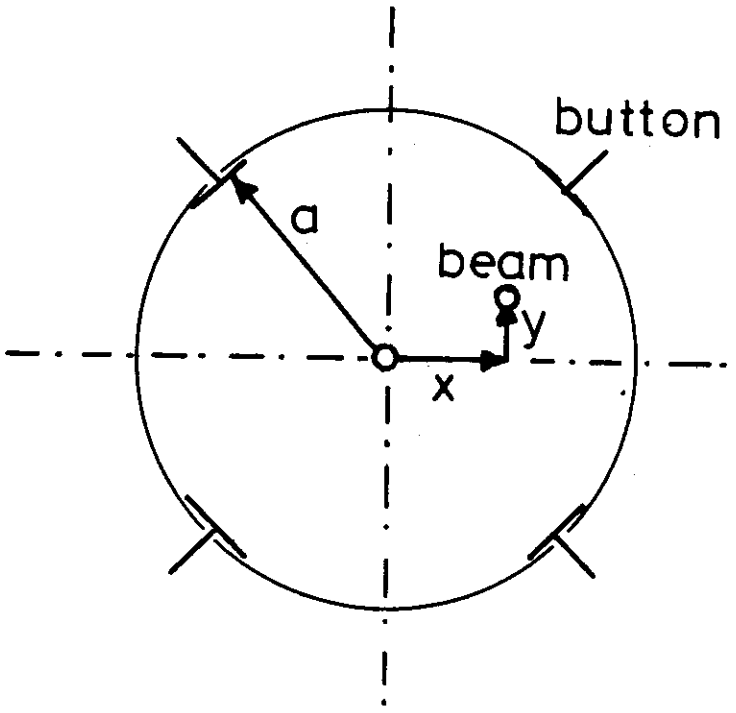

Fig. 3.10 Position sensitivity for a circular chamber

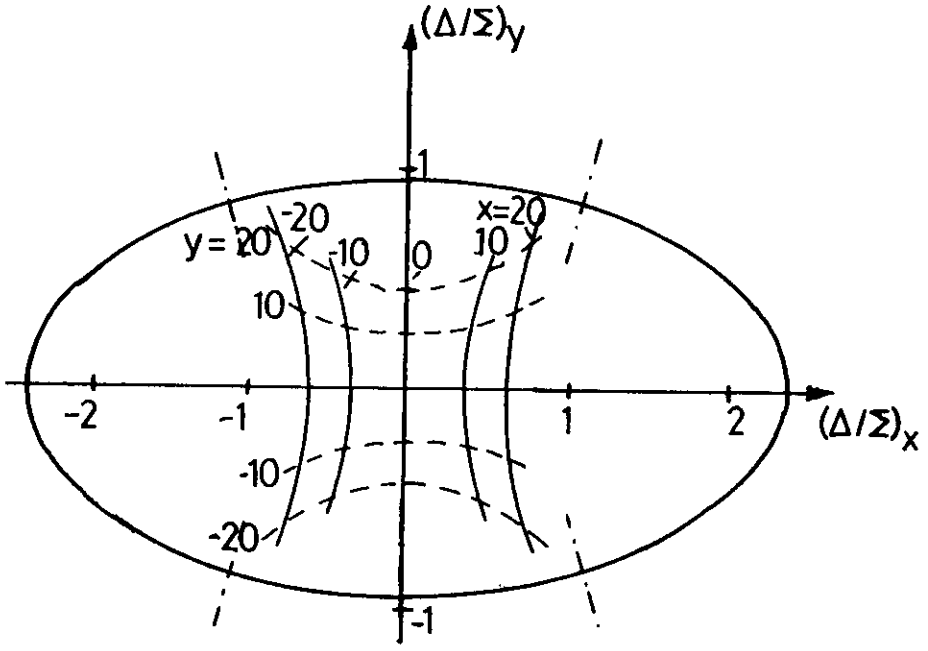

Fig. 3.11 Measured horizontal and vertical position signals $(\Delta/\Sigma)_x$ and $(\Delta/\Sigma)_y$ as a function of beam positions x and y in mm (simulated by the central conductor). For a beam position x = 10 mm, y = 0 mm we find $(\Delta/\Sigma)_x$ = 0.35 and for x = 0 mm, y = 10 mm we find $(\Delta/\Sigma)_y$ = 0.26.

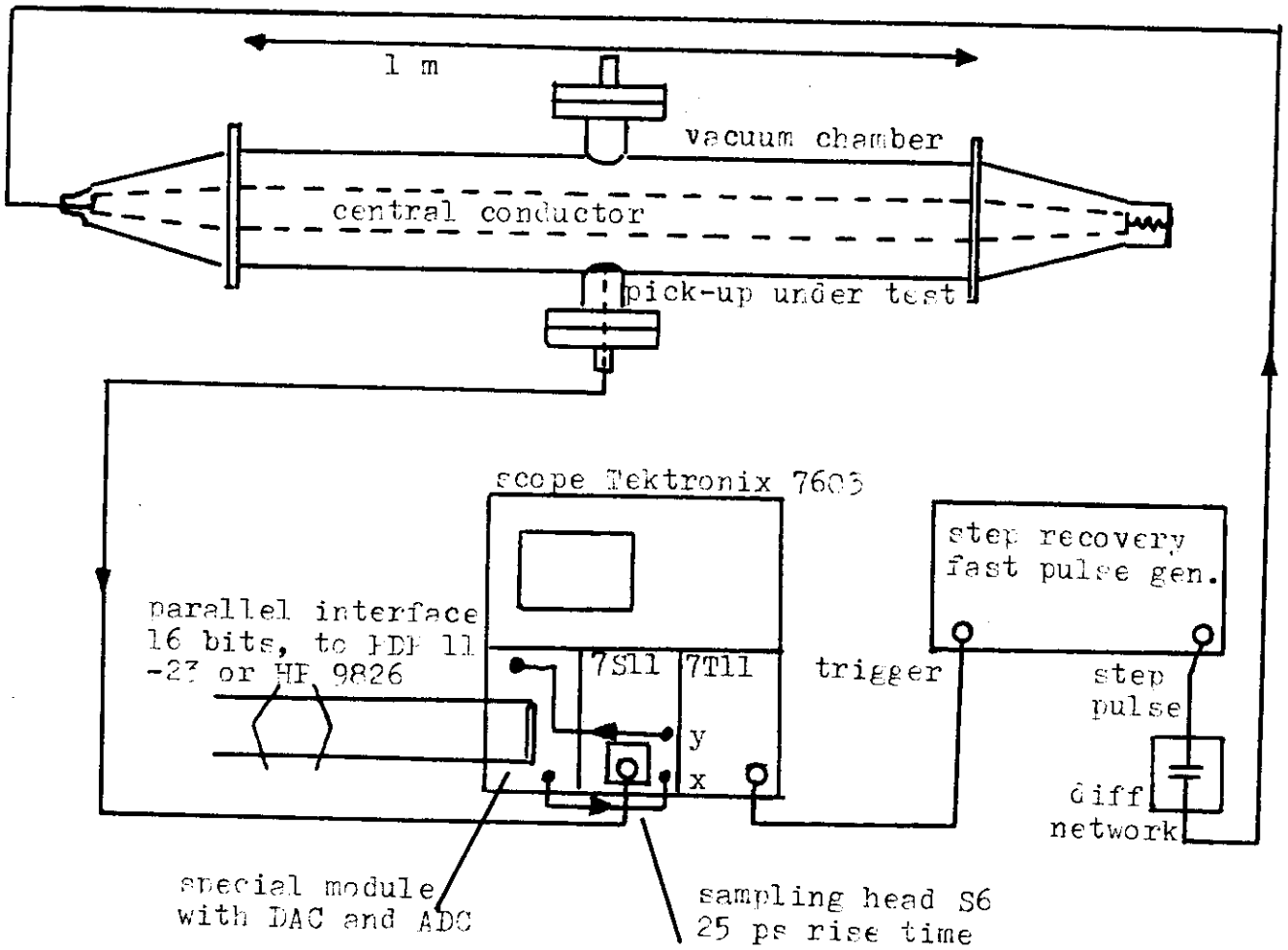

Fig. 3.12 Test set-up.

3.6 Test bench and set-up

A test set-up has been designed and built in collaboration with the LEP RF group (H. Henke), for the electrical test of the beam position monitors and other elements of the vacuum chamber. Figure 3.12 represents the block diagram of the set-up. The pulse generator gives pulses corresponding to the LEP bunch signal, 5 V_{peak} and 90_{ps} duration (mid-height) or step function with 90_{ps} rise time and 27 V_{peak}. The pulses are produced by step-recovery diodes. Figures 3.13 and 3.14 show on the top the generator pulses and their spectra.

The test line is made of a pipe with the LEP chamber inner profile and a circular central conductor having either 50 Ω (for maximum coupling) or higher impedance (200 Ω) for higher mode waveguide excitation or beam position simulation. The set-up can also be used for comparative measurements[36-39] whereby a blank chamber response is compared with that of a chamber containing the object to the measured.

Button electrodes transfer impedance, coupling between adjacent objects mounted on the vacuum chamber, longitudinal and transverse impedances are measured[36-39]. The time domain pulse signal is first sampled and digitalised with a modified Tektronix sampling scope. 1024 points are recorded with 12 bits resolution. The system rise time is 25 ps corresponding to a bandwidith of 13 GHz.

A parallel interface is used between the sampler and a computer which is either PDP 11-23 or HP 9826. The sampler digital converter is fed by the scope power supply. It is very stable and reproducible, allowing comparative measurements by successive acquisition.

The computer calculates the FFT (see Fig. 3.13) and will calculate the transfer function for optimum resolution of low coupling or low loss effects, like the bellow assembly perturbation.

The tests made on electrode models have shown that the electrode diameter d is not a critical factor even for d ≈ the bunch length.

Fig. 3.13 shows the pulse response of the electrode and 3.14 its step response, with time constant R_0C_e, corresponding to the low frequency response discussed in chapter 4.

These results demonstrate the feasibility of a very wide band monitor, up to at least 13 GHz, with a button electrode of 26 mm diameter.

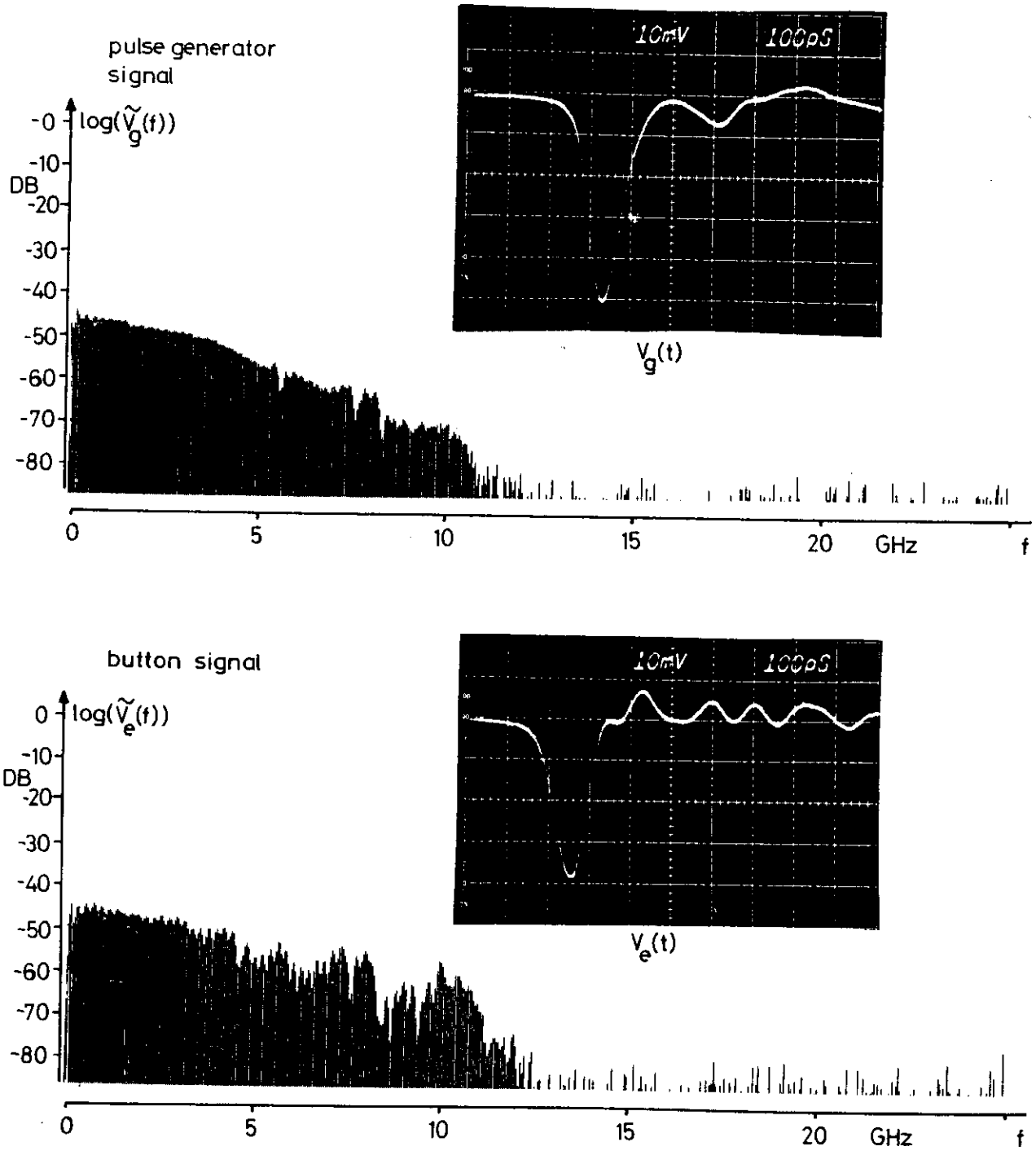

Fig. 3.13 Response of the electrode in time and frequency domain $V_e(t)$, $\tilde{V}_e(f)$ to a pulse $V_g(t)$, $\tilde{V}_g(f)$ from the generator which simulates the beam.

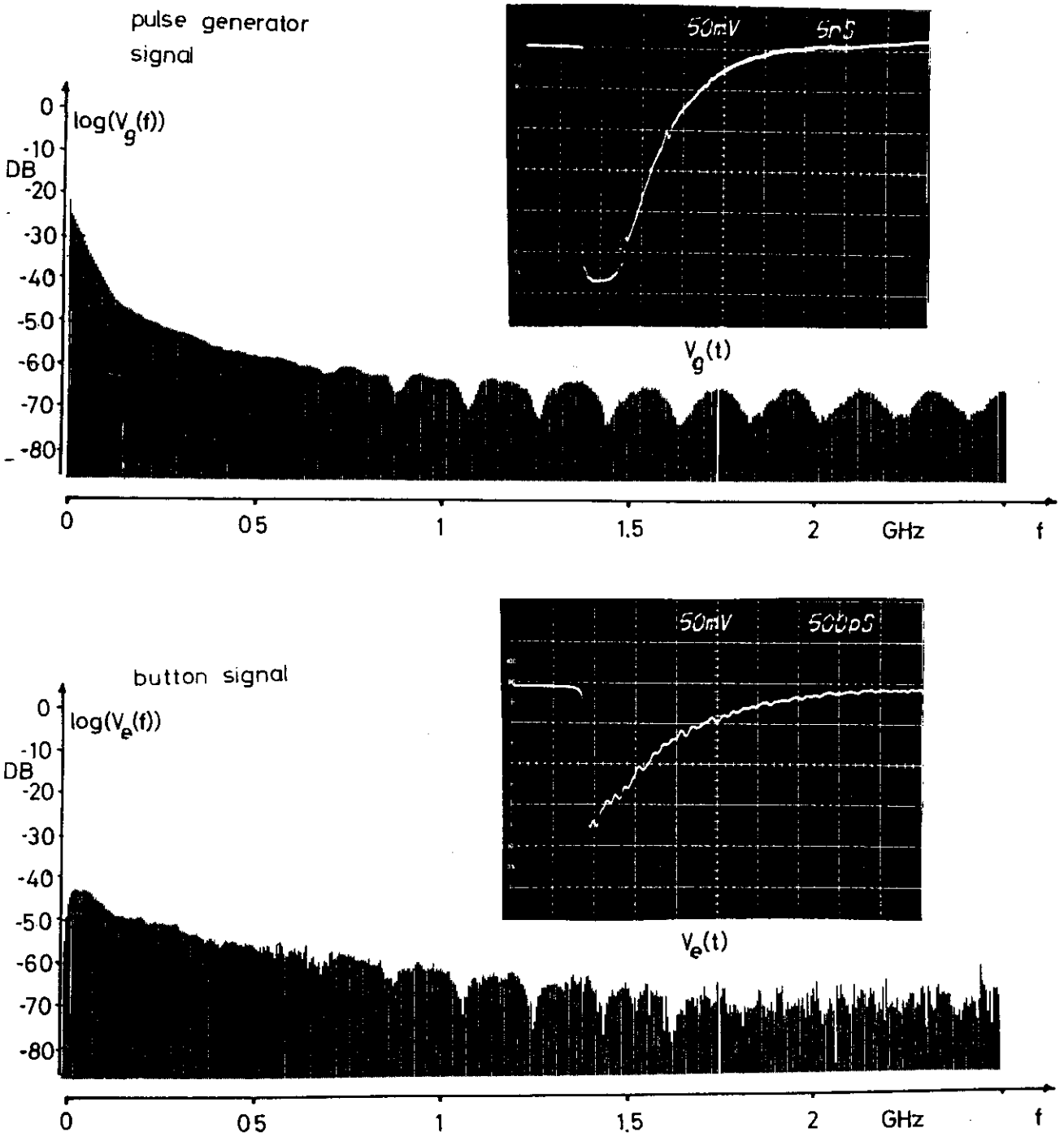

Fig. 3.14 Response of the electrode in time and frequency domain $V_e(t)$, $\tilde{V}_e(f)$ to a step with time constant $R_o C_e$ from the generator.

4. Beam signal characteristics

4.1 Button electrode and cable transfer impedance

Since the use of an active or passive high impedance transmission system is not possible due to losses or radiation damage, the only feasible solution is a coaxial cable of R_o = 50 to 75 Ω.

The equivalent circuit for a button and the cable is then a simple R-C high-pass filter shown in Fig. 4.1.

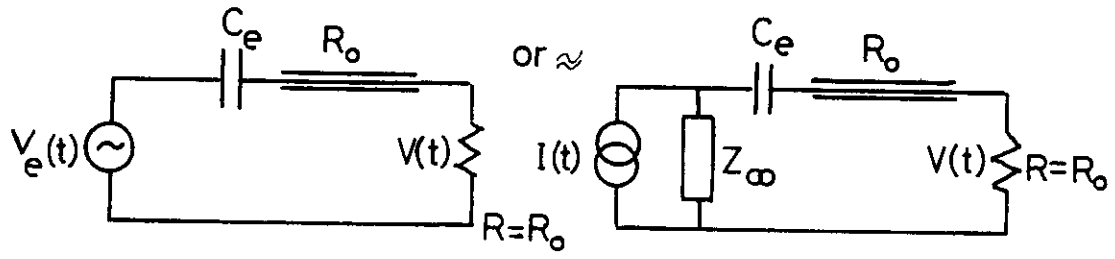

Fig. 4.1 Equivalent circuits relating the voltage V(t) at the end of the cable to the voltage $V_e(t)$ at the button and to the beam current I(t).

Expressed in the frequency domain:

from equation 3.1

$$\tilde{V}_e(f) = \tilde{I}(f)Z_\infty \qquad (4.1)$$

and

$$\tilde{V}(f) = \tilde{I}(f)Z(f) \qquad (4.2)$$

$$Z(f) = \frac{Z_\infty}{1 + \frac{1}{j2\pi f R_o C_e}}$$

with lower cut off frequency

$$\left.\begin{aligned} f_c &= \frac{1}{2\pi R_o C_e} \\ |Z(f)| &= \frac{Z_\infty}{\sqrt{1 + (f_c/f)^2}} \\ \phi_z &= \arctan(f_c/f) \end{aligned}\right\} \qquad (4.3)$$

For C_e = 17 pF and R_o = 50Ω we get f_c = 190 MHz and
for C_e = 15 pF, f_c = 210 MHz.

Figure 4.2 shows this measured low-pass characteristic with a network analyser. The measured high frequency attenuation of -43 dB gives the measured Z_∞ = 0.35 Ω of the electrode-monitor assembly. The same result is obtained by comparing Fig. 3.13 and Fig. 3.14.

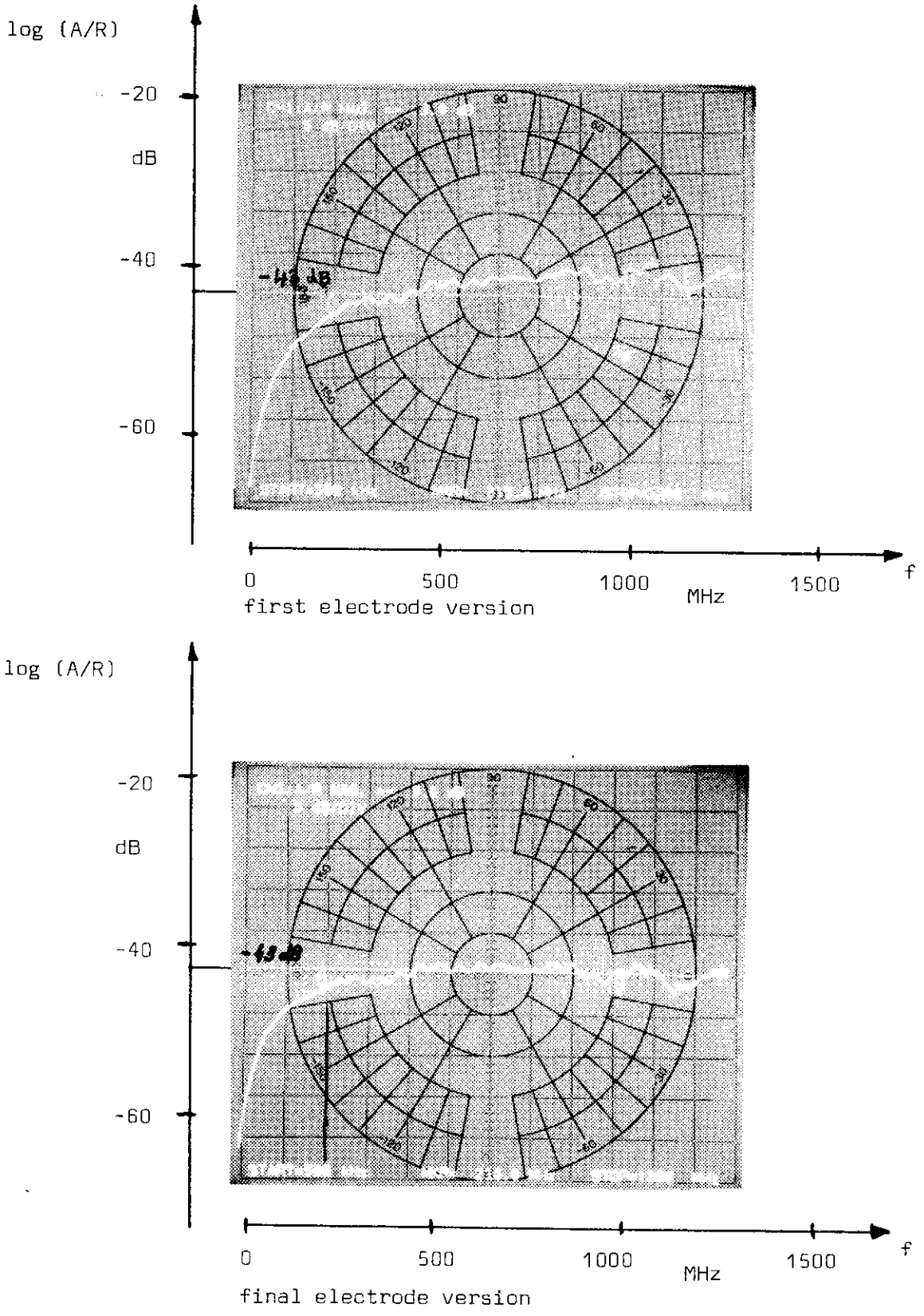

Fig. 4.2 Transfer function between the generator signal R sent through the central conductor of the test set-up (Fig. 3.12) and the signal A obtained from the button with Z_∞= 0.35 Ω and C_e = 17 pF.

4.2 Frequency response of a button to a single Gaussian bunch

With the equivalent circuit given in section 4.1 and equation (4.2)

$$\tilde{V}(f) = \tilde{I}(f) \cdot Z(f)$$

where $\tilde{I}(f)$ is defined by equation (1.2) and $Z(f)$ by equation (4.3).

It is important to see that even for a low impedance transmission (R_o = 50 Ω) $f_c \ll f_s$, where f_s is the rms frequency of the bunch spectrum (1.2).

$$f_s = \frac{c}{2\pi\sigma}$$ see table 1.1.

The product of the 2 curves $\tilde{I}_b(f)$ and $Z(f)$ clearly shows three regions (see Fig. 4.3).

(i) $0 < f < f_c$

$$Z = Z_\infty \frac{x}{\sqrt{1 + x^2}} \quad \text{with } x = f/f_c; \quad \text{for } x \ll 1,\ Z \to Z_\infty \cdot x;$$

Therefore for $f \ll f_c$, Z is proportional to R_o and f and becomes independent of C_e, i.e. the equality between button capacitance is no longer critical but the matching of the four cable impedances becomes critical.

(ii) $f_c < f < f_s$
where $V(f)$ is almost constant but inversely proportional to C_e.

(iii) $f_s < f$ where $\tilde{V}(f)$ is affected by the bunch length and by the electrode resonances.

In fig. 4.3 the voltage $\tilde{V}(f)$ of the button voltage is shown for different cable attenuations for a bunch of 1 mA current. The bunch spectrum $\tilde{I}(f)$ is shown in the same figure.

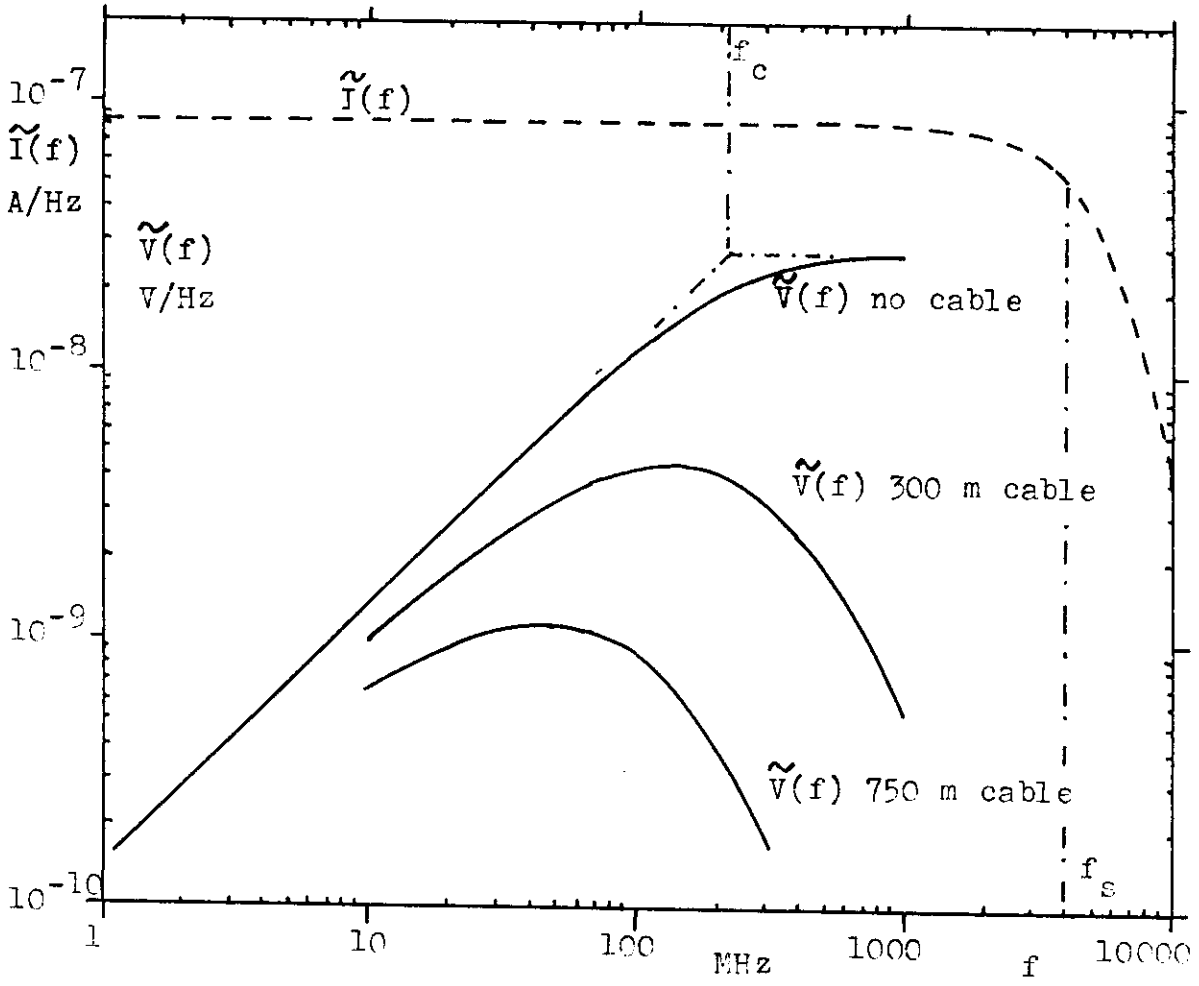

Fig. 4.3 Current spectrum $\tilde{I}(f)$ and voltage spectrum $\tilde{V}(f)$ of the button signal for a single bunch with $5.56 \cdot 10^{11}$ particles (I_o = I mA) with Z_∞= 0.3 Ω, C_e = 15 pF and different length of CK50 cable.

4.3 Frequency response of the button to a circulating beam

With k_b = four equidistant bunches, the time structure appears as a convolution of the Gaussian bunch current (1.1) and a Dirac comb $\sum\delta(t-nT_b)$ with $T_b = 1/k_b f_{rev} = 22.23$ μs. The spectrum of this current of the k_b equal bunches consists of lines space by $k_b \cdot f_{rev} = 45$ kHz with amplitudes given by (1.3) and shown in Fig. 1.2.

The peak current signal passing through a theoretical rectangular band-pass filter $f_o \pm \Delta f$ is

$$I(f_o) = 2\tilde{I}(f_o)2\Delta f = \frac{4\, I_o \Delta f}{k_b\, f_{rev}} \exp\left(-\frac{f_o^2}{2f_s^2}\right) = 4Q_b \Delta f \exp\left(-\frac{f_o^2}{2f_s^2}\right) \quad (4.4)$$

where $Q_b = N_b e$ is the charge per bunch and $2\Delta f/(k_b f_{rev})$ gives the number of spectral lines falling into the pass band of the filter. The factor 2 in front of $\tilde{I}(f_o)$ in (4.4) is due to the fact that $\tilde{I}(f_o)$ contains positive and negative frequencies. Note that (4.4) gives the peak current; if more than one line falls into the pass band, the signal obtained will beat in time.

5. Basic choices for signal transmission

5.1 Minimum of active electronics in the tunnel

Even if the radiation level in the tunnel due to synchrotron radiation could be reduced by some shielding around the electronics, the maintenance of such an electronics along the 27 km of LEP circumference is a difficult problem.

5.2 Standard equipment for all the position monitors

For cost and maintenance purposes, it is worthwhile having identical modules for all the monitors. To reduce the dispersion in cable attenuation

between pick-ups without using repeaters, one should not transmit the upper part of the spectrum.

5.3 Two separate cables per pick-up

It will be shown that the signal level is relatively small. Any passive multiplexing devices (hybrid, directional couplers) would introduce insertion losses. Fast switches using active electronics might not withstand the high radiation level. In both cases it is not easy to solve the cross-talk problems.

Having two separate cables per pick-up (three cables for the few pick-up stations in the vicinity of the interaction region with horizontal and vertical read-out) is a reliable solution since bad contact eliminates only one pick-up. Using the alcoves for signal processing reduces the cable cost by a factor 3, compared to having only one data centre near the intersection. A possible arrangement of the signal cables is shown in Fig. 5.1.

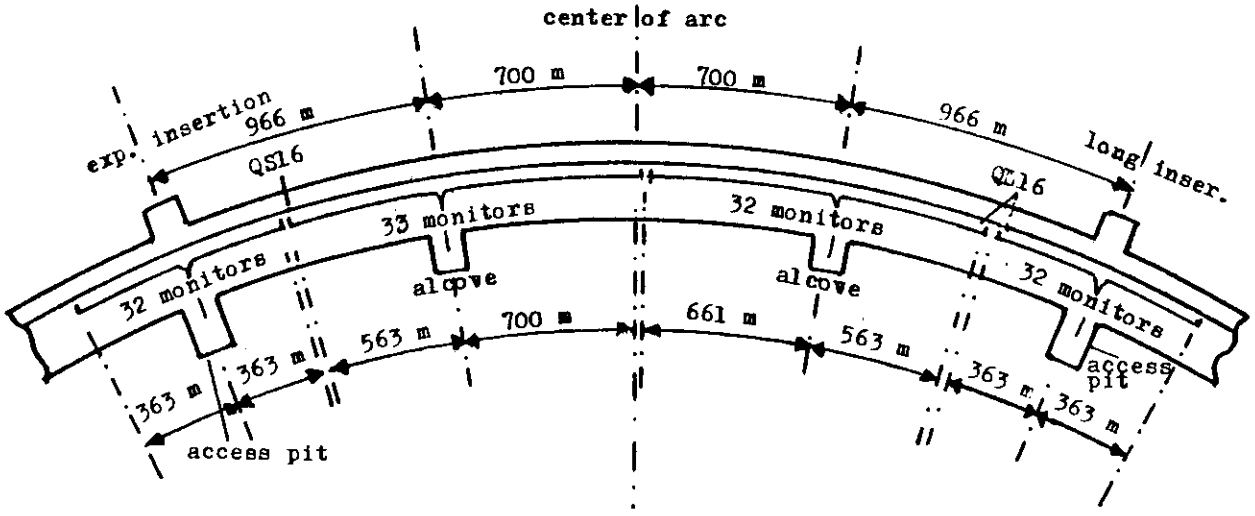

Fig. 5.1 Possible layout of the cabling for the monitors. The distance indications refer to a path along the beam and are only accurate to about a quadrupole length.

5.4 Choice of frequency for the narrow band transmission

If a narrow band signal transmission is chosen the best frequency f_o results from a compromise between:

- the signal at the pick-up level which increases with f up to the frequency corresponding to Z_∞;
- the signal at the receiver level (alcove or pit) which decreases with the attenuation along the cables. In the alcove solution the cable lengths are between 20 m and 750 m. Without the use of the alcoves, it would extend to 1700 m. The band-width Δf determines the pulse duration

$$\Delta T \approx \frac{2.2}{\pi \Delta f}$$

and amplitude at the output of a Bessel filter. The larger is Δf, the larger is the signal and the smaller ΔT. The number N_p of periods T_o inside ΔT influences the quality of the synchronous demodulation. The SPS experience shows N_p must be ≥ 5.

Number N_p periods and cable attenuations are shown in table 5.1 for different frequencies f_o.

f_o MHZ	$1/f_o$ ns	Δf MHZ	ΔT ns	N_p	α(CK50) db/km
200	5	2	350	60	43
100	10	2	350	30	28
50	20	2	350	15	18
20	50	2	350	6	12
10	100	2	350	3	8

Table 5.1. Number N_p of oscillation periods within a signal pulse and cable attenuation for different transmission frequencies f_o.

If in the future of LEP the number of bunches is increased it could be worthwhile if f_o is a divider of the RF (f_{RF} = 352.21 MHZ) included in the harmonic number ($h = 31320 = 2^3 \times 3^4 \times 5 \times 29$) and keeping the periodicity of 8. The frequency

$$f_o = \frac{f_{RF}}{15} = 23.480 \text{ MHz}$$

seems an interesting compromise. It would result in only 10 dB attenuation difference between signals entering into the same alcove. Other frequencies being a multiple of f_o could also be used.

Having chosen f_o and Δf, the first signal treatment is to select the band pass by a filter and to add the button signals 2 by 2 to get one plane per pick-up. This can be done by two 180° hybrids having optimimum characteristics (insertion loss, isolation, VSWR, amplitude and phase balance) only in the required bandwidth.

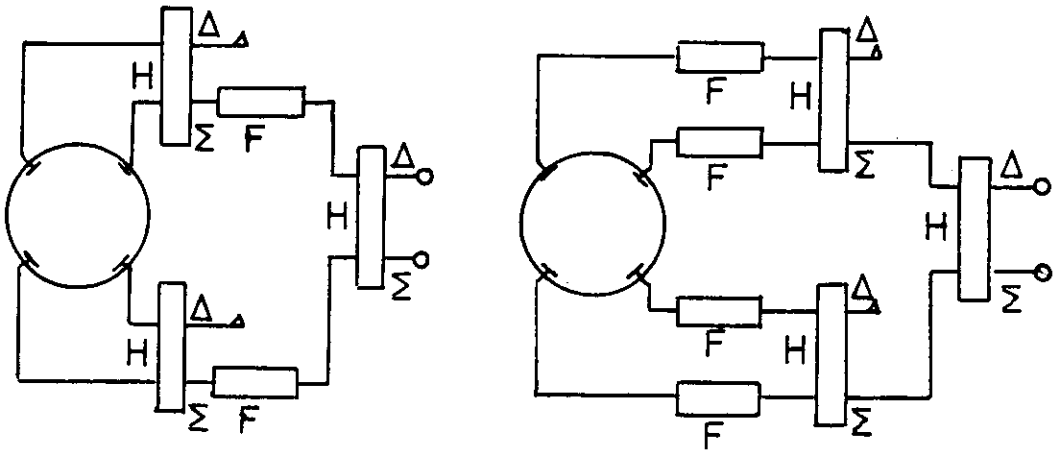

Fig. 5.2. Solutions using two or four filters; F - filter, H - hybrid.

A solution with 2 filters is possible only if there are no saturation effects in the hybrids by the large peak current before filtering. Otherwise the solution of filtering before the hybrid must be taken which needs four filters (see Fig. 5.2).

To avoid multiple reflections between the filter input and the button for frequencies higher than the bandwidth, leading to possible modulation inside the bandwidth, the filter inputs must be matched to these high frequencies.

5.5 Cable losses consideration for the wide-band transmission with low-pass

In the case of low-pass filtering for pulse lengthening, added to the high-pass characteristic of the button electode, the overall system becomes a broad "band-pass" filter to which the cable losses as function frequency have been added.

Fig. 5.3 shows the overall frequency response for different CK50 cable lengths. In this case the low-pass cut-off frequency should coincide with the low-pass effect of the cable losses in order to keep a as large Δf as possible, which in turn will determine the peak amplitude of filtered pulse and optimise the energy transmission. If one considers the 750 m length, the low-pass filter cut-off should be around 100 MHz. This will be discussed further in section 6.2.

5.6 Comparison between individual electrode signal treatment and that of Δ and Σ

Two possibilities of signal treatment are investigated:

a) After summing buttons 1 and 4 and buttons 2 and 3, the two sum signals A and B are transmitted by two cables to two electronic chains (Fig. 5.4). If the amplification or attenuation in the two chains has errors of $\pm\varepsilon$ the signals A' and B' can have errors of the form:

$$A' \propto A(1+\varepsilon) \text{ and } B' \propto B(1+\varepsilon).$$

The ratio between the difference and sum signals formed thereafter will have an error

$$\frac{\Delta}{\Sigma} = \frac{A(1+\varepsilon) - B(1-\varepsilon)}{A(1+\varepsilon) + B(1-\varepsilon)} \approx \frac{A-B}{A+B} + \varepsilon$$

assuming $\frac{A-B}{A+B} \ll 1$.

The gain uncertainty ε appears as an absolute error in the position measurement

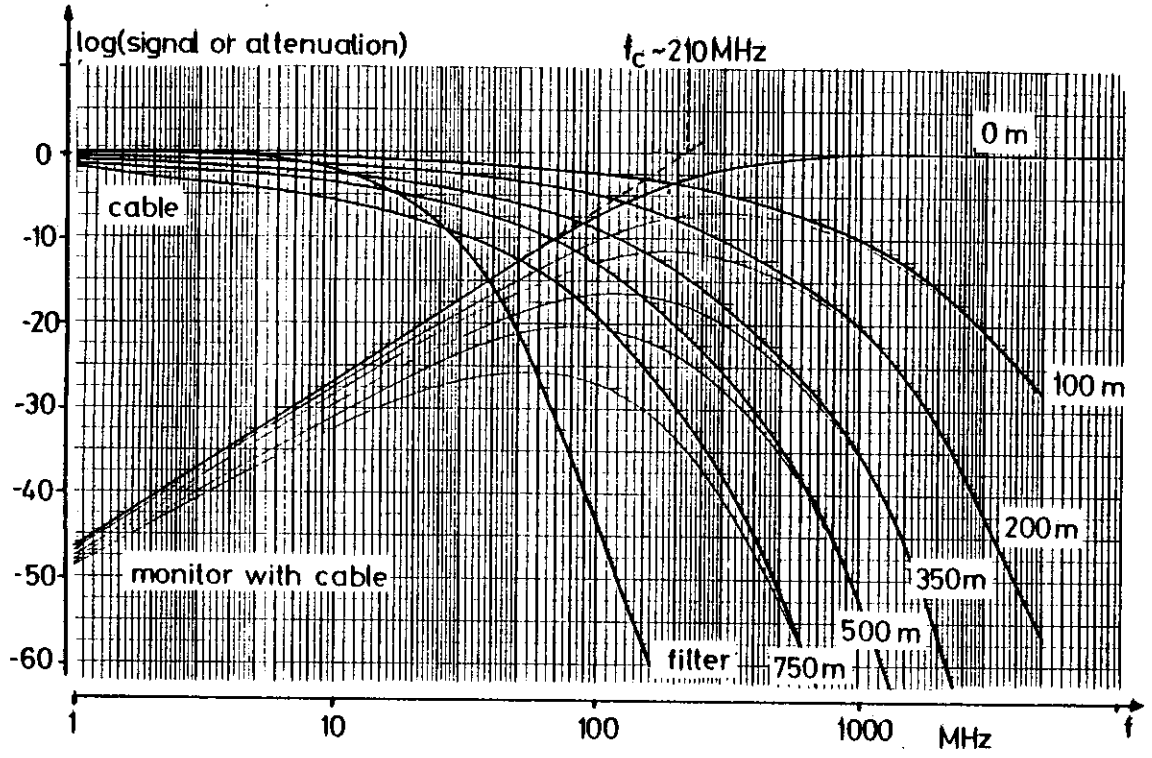

Fig. 5.3. Frequency response of different lengths of CK50 cable, of the low-pass filter and of the monitor with cable for C_e = 15 pF.

b) As a second possibility the difference and sum of the two signals A and B are taken locally and the resulting signals are amplified after,

$$\frac{\Delta}{\Sigma} \approx \frac{A-B}{A+B}(1 + 2\varepsilon) \quad \text{for } \varepsilon \ll 1.$$

The gain uncertainty ε enters here as a relative error into the position measurement, or scaling factor error.

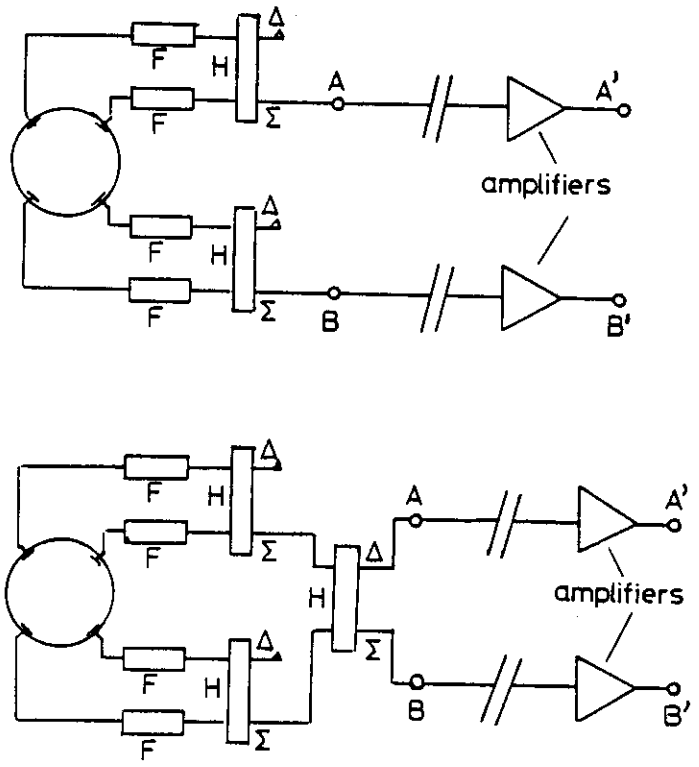

Fig. 5.4. Two possible ways of signal transmission for the example of a vertical position monitor; top - the two sum signals of the upper and lower buttons are transmitted individually; bottom - the sum and difference signals are formed locally by a hybrid and transmitted thereafter.

5.7 Approaches of signal treatment

In the next chapter two approaches for the signal treatment will be considered.

In the first possibility the signals from the buttons will pass through a band-pass filter $f_o \pm \Delta f$. Thereafter, the sum signals A and B of the

button pairs (1,4) and (2,3) pass to a second hybrid where the signals A-B and A+B are formed as described in the option b) in section 5.6 and shown in Fig. 6.2. These two signals are then sent to the alcove for signal treatment. Here a synchronous detector could be used to measure the amplitudes of the difference and sum signals Δ and Σ. This detection requires a good phase stability between the two signals; SPS experience[40] shows that the phase indeed stays very stable after the cables are adjusted.

The second possibility to be investigated uses a low-pass filter for each of the 4 buttons. The sum of the pairs of buttons (1,4) and (2,3) is thereafter formed and these two signals are amplified and sent by cables to the alcove f_o-detection as described in the approach a) in section 5.6 and shown in Fig. 5.4. The amplitude of the two signals is measured preferably with a peak detector having a threshold at very low voltage. ISR experience with the $\bar{p}$ system shows that such signal processing is feasible in accelerator environment[41].

6. Signal level and expected resolution

6.1 Narrow band signal processing approach

6.1.1 Button signal level

Knowing the frequency response of a button and the basic choices, the signal level can be estimated for a low impedance (= 50Ω) transmission at $f_o \pm \Delta f = (23.5 \pm 2)$ MHz.

For $R_o = 50\Omega$ $\quad C = 15$ pF $\quad f_{3dB} = 210$ MHz $\quad Z_\infty = 0.30\Omega$

From equation 4.3 $\left|Z(f_o)\right| = 0.033\Omega$.

A good approximation of the peak voltage V_c of the signal in the bandwidth $f_o \pm \Delta f$ is

$$V_c = \int_{-\Delta f}^{+\Delta f} \tilde{V}(f_o)\, df \cong 2\tilde{V}(f_o) 2\Delta f \qquad (6.1)$$

with equation 4.5 $\tilde{V}(f_o) = \tilde{I}(f_o) \cdot Z(f_o)$

$$V_c = 4.Q_b \cdot \Delta f \cdot Z(f_o)$$

with Q_b being the charge per bunch. The first factor of 2 in (6.1) is due to the fact that the spectrum $\tilde{V}(f)$ contains positive and negative frequencies.

6.1.2 Synchronous demodulation sensitivity

The synchronous demodulation[20] is a device with very good noise rejection (Fig. 6.1).

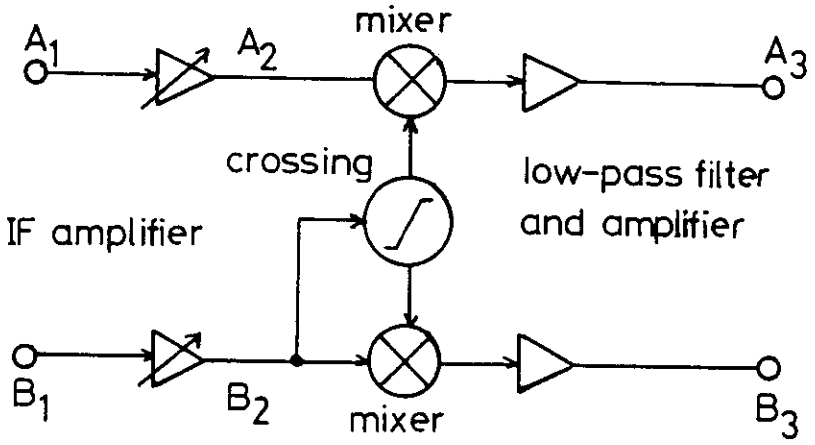

Fig. 6.1 Synchronous demodulation.

Experience gained at SPS[33] has shown that signal level up to 6 dB above the white noise level in the bandwidth can be detected on the A channel providing the B signal level at the input of the zero crossing is large enough : typically $B_2 > 10$ mV ptp while the maximum for B_2 is $\leq$ 700 mV ptp.

The input signals A1 and B1 can be amplified by programmable gain IF amplifier with a gain up to 60 dB. With 50Ω input impedance the thermal noise in $2\Delta f$ is $V_N = (4kTR_o\ 2\Delta f)^{1/2} = 1.8$ μv rms. With a 6 dB noise figure for the IF amplifier, V_N becomes 3.6 μV rms or 10.8 μV peak (3σ). Then the minimum signals could be 20 μV peak on input A (6 dB above noise) and 30 μV peak on input B (10 db above noise for synchronous demodulation).

6.1.3 Signal levels for Δ and Σ transmission

With a 4-button pick-up to give the position in one plane (horizontal or vertical), the sum and difference signals can be formed with a circuit as shown in Fig. 6.2. It uses bandpass filters F with $f_o \pm \Delta f = (23.5 \pm 2)$MHz followed by 180° hybrids H_1 and H_2. With a centred beam and a signal V_c at each button, the sum signals are

$$A = \Sigma_{1+4} = B = \Sigma_{2+3} = \sqrt{2}\, V_c$$

$$\Sigma_{Total} = 2\, V_c\ ,\quad \Delta_{A.B} = 0.$$

The full length ΔT of the pulse is

$$\Delta T \approx \frac{2.2}{\pi \Delta f} = 350 \text{ ns.}$$

The estimated signals V_c at the buttons as well as the sum and difference signals Σ_R and Δ_R after 750 m of CK50 cables are listed in table 6.1 for different conditions. For the difference signal, a beam displacement of 0.1 mm was assumed. Under nominal conditions, the signals are large enough (IF-gain) but at injection the Δ signal is too low for this small displacement.

Condition	N_b	Q_b AS	V_c mV	Σ_R mV	Δ_R μV
1 injected pulse	$2.2.10^{9}$	$3.5.10^{-10}$	0.09	0.07	0.19
nominal current	$4.2.10^{11}$	$6.7.10^{-8}$	17.7	13.1	36.8

Table 6.1 : Signal level V_c at the button and Σ_R after 750 m of CK50 cable for different conditions. The Δ_R signal is evaluated for a beam displacement of 0.1 mm.

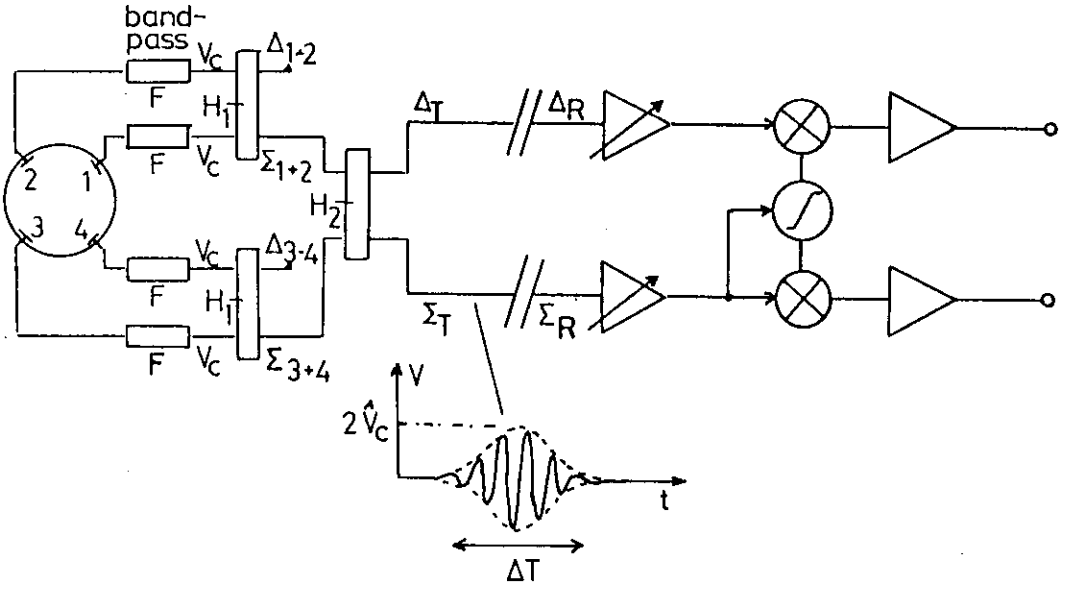

Fig. 6.2 Circuit for the narrow-band signal treatment.

More precise data can be obtained using the curves in Fig. 4.2. Taking the attenuation of $\tilde{V}(f)$ in 750 m cable length into account, an inverse Fourrier transform can be performed after the signal has passed through a band pass filter at frequency $f_o \pm \Delta f$.

By keeping f_o high and Δf small, parasitic signals can usually be avoided and the remaining noise is of thermal origin. Estimated signal levels and resolution are shown in Table 6.2 for injection conditions. The noise peak voltage V_{noise} listed is measured at the end of the long signal cable and takes the cable attenuation of the noise of an amplifier at the monitor into account.

f_o/f_{RF}	f_o MHz	$\tilde{V}(f_o)$ pV/Hz	Δf MHz	ΔT ns	$\Sigma = 2V_c$ µV	$\hat{V}_{noise}$ µV	$\Sigma/\hat{V}_{noise}$	Δx mm
1/15	23.48	4.0	2	350	65	6.0	10.8	3.3
1/5	70.44	4.3	4	175	137	3.8	36.0	0.9
1/3	117.40	3.2	8	87.5	207	2.7	76.5	0.5

Table 6.2. Signal level, noise level and spacial resolution of the monitor as a function of the filter frequency f_o for injection conditions with $2.2 \cdot 10^9$ particles ($3.5 \cdot 10^{-10}$ AS) per pulse. For the buttons $R_o = 50\Omega$, $Z_\infty = 0.3\Omega$, $C_e = 15$ pF was assumed and a ratio of $\Delta/\Sigma x = 0.028$/mm was used to calculate the resolution Δx which is defined as the displacement giving a signal-to-noise ratio of unity.

6.1.4 Possible improvements

The following improvements could be considered :

a) Introduction of two 30 dB preamplifiers per monitor in the tunnel, for the injection condition (Fig. 6.3)

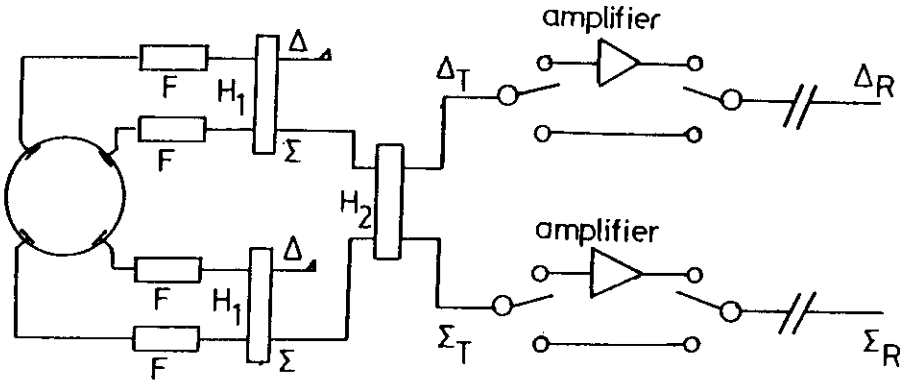

Fig. 6.3 Possible improvement by switching in head amplifiers for low beam intensities.

b) Combining the filter with an impedance transformer

c) Transmission via 90° hybrid and a phase discrimination as receiver[42)]

d) Transmission of two (or more) monitor signals on two (or more) frequencies[42)], to reduce the cable cost.

6.2 Wide-band signal processing approach

6.2.1 Circuit principle

The idea of this approach is to extract as much power out of the available spectrum as possible and to compare it with the equivalent input noise signal of the best feasible amplifier. As already stated in 5.5, the cut-off frequency of the low-pass filter should not be beyond the cut-off due to the cable losses (Fig. 5.3) in order to maintain quite similar response for all cable lengths. This wide-band solution allows a shorter length for the filtered pulse than for the detected envelope of the narrow band solution and hence facilitate the signal treatment of monitors closer to the intersections without interference for the electron and positron signals. The analog signal processing circuitry is simpler and may present reliability advantages. But, on the other hand, it may be more sensitive to external parasitic signals.

The equivalent circuit of this approach is shown in fig. 6.4

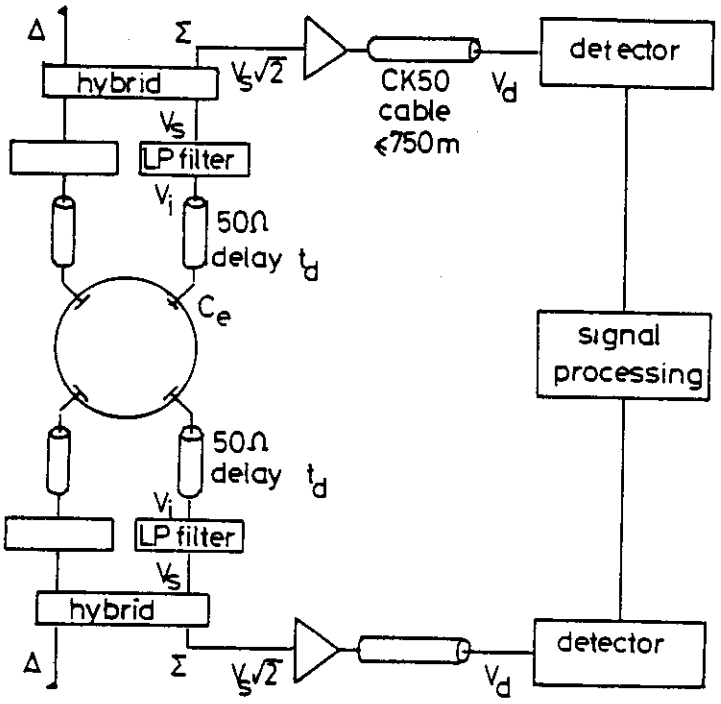

Fig. 6.4 Circuit for the wide-band signal processing.

The transfer function of the system can be represented by two frequency functions, the frequency response of the filter and the response of the pick-up and cable, see fig. 5.3.

6.2.2 Time domain response

The time domain response of such a system (fig. 6.5) can be evaluated in a simplified way using the following approximate relations[43,44]. For a given beam induced input pulse of amplitude $\hat{V}_i$ and duration $t_b \approx \sqrt{2\pi}.\sigma/c$ into the low-pass filter with a cut-off frequency f_l the amplitude of the output pulse $\hat{V}_s$

$$\frac{\hat{V}_s}{\hat{V}_i} \approx \frac{t_b}{t_r} \qquad (6.2)$$

where t_r is the low-pass filter rise time

$$t_r \approx \frac{0.35}{f_1} \tag{6.3}$$

The output pulse has a length t_r and a rise time $t_r/2$. The input signal $V_i(t)$ to the filter is the unloaded electrode voltage V_e differentiated and multiplied by the R_oC_e time constant

$$V_i(t) \approx R_o C_e \frac{dV_e}{dt} \tag{6.4}$$

for frequencies smaller than the high-pass electrode-cable cut-off frequency f_o

$$f_o = \frac{1}{2\pi R_o C_e}$$

The amplitude $\hat{V}_s$ of the total response is obtained from (6.2), (6.3) and (6.4)

$$\hat{V}_s \approx \hat{V}_e \frac{2t_b R_o C_e}{t_r^2} \approx \hat{V}_e \, 16.3 \, t_b \, R_o \, C_e \, f_1^2 \tag{6.5}$$

From (1.1) and (3.5) we get for the peak voltage $\hat{V}_e$ due to one button

$$\hat{V}_e = \hat{I} \, Z_\infty \approx \frac{Q_b}{t_b} Z_\infty$$

with $Q_b = N_b e$ being the charge per bunch. This gives for the peak voltage at the output of the low-pass filter

$$\hat{V}_s = 16.3 \, Q_b \, Z_\infty \, R_o \, C_e \, f_1^2 \tag{6.7}$$

The approximate form of this pulse is shown in fig. 6.5. It should be noted that Z_∞ is proportional to $1/C_e$ (3.5) and $\hat{V}_s$ is therefore independent of the electrode capacity C_e but is proportional to the cable impedance R_o and to the square of the cut-off frequency f_1. This is important for the precision of the system.

6.2.3 Low pass filter

Such a filter has been built for a f_1 = 20 MHz. Its circuit is given on Fig. 6.6. Its calculated input impedance is far from being 50Ω over the total frequency domain of the electrode signal spectrum. This will produce reflexion of the non absorbed part of the pulse energy which will be sent back toward the electrode capacity which also does not match the cable impedance. This will produce oscillations, depending on the cable length and its propagation delay t_d, which may fall into the frequency band of the system. After simulation in the lab., it was decided to match the low-pass filter input impedance with a resistive high pass to absorb the unused part of the spectrum. Figure 6.7 shows the result of the adaptation which makes the frequency characteristic of the processing chain independant of the cable length. Figures 6.8 and 6.9 present the overall transfer function in the frequency domain. Figure 6.10 shows the overall time domain response and its FFT transform for the pseudo step function sent on the line of the test set-up (Fig. 3.11).

6.2.4 Optimisation of the system power transmission

In order to optimise the analog processing chain, the output voltage has been calculated for different cut-off frequencies. In Table 6.3, the resulting voltage $\sqrt{2}\ \hat{V}_S$ from the sum signal of two buttons and the pulse length are listed.

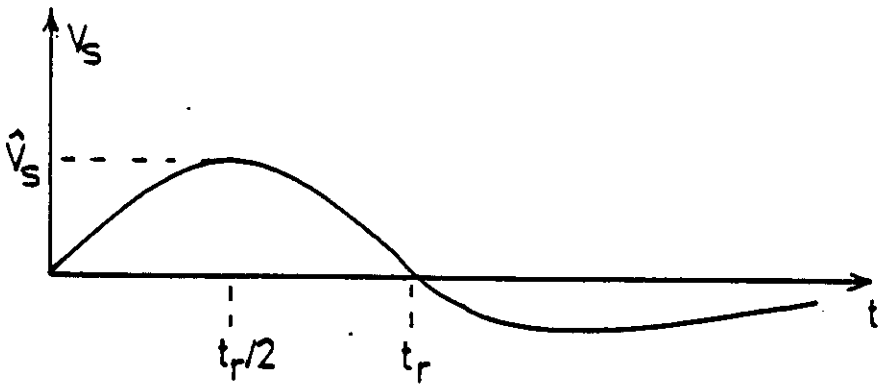

Fig. 6.5 Pulse form in a wide-band read-out system.

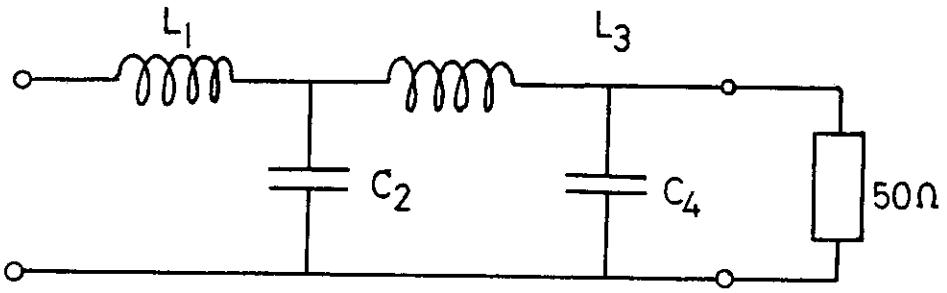

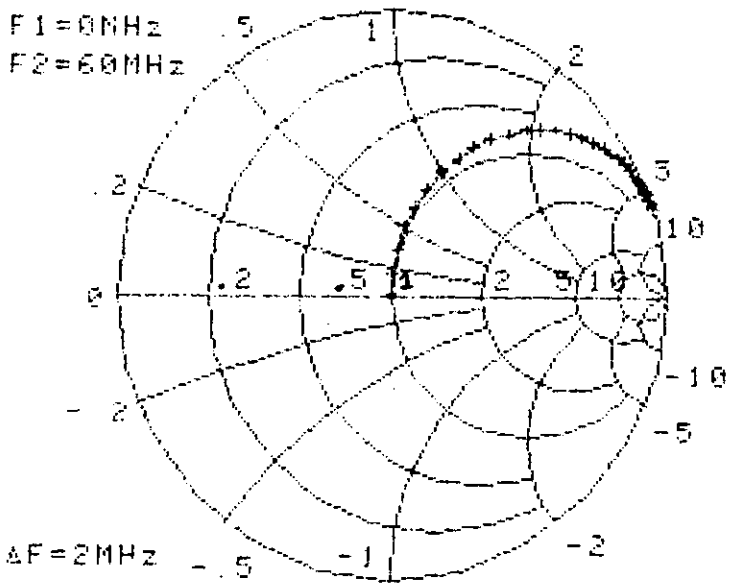

Fig. 6.6 Circuit of the Gaussian low-pass filter with f_1 = 20 MHz, R_o = 50Ω using L_1 = 0.8935 µH, C_2 = 148.35 pF, L_3 = 0.21095 µH, C_4 = 28.2 pF and the Smith chart of its input impedance normalized to 50Ω.

4.2.83

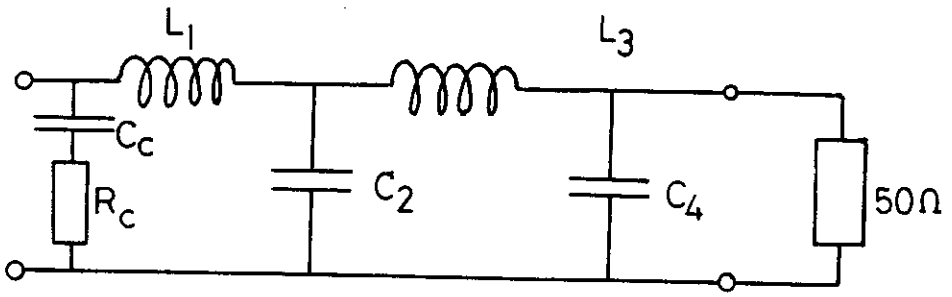

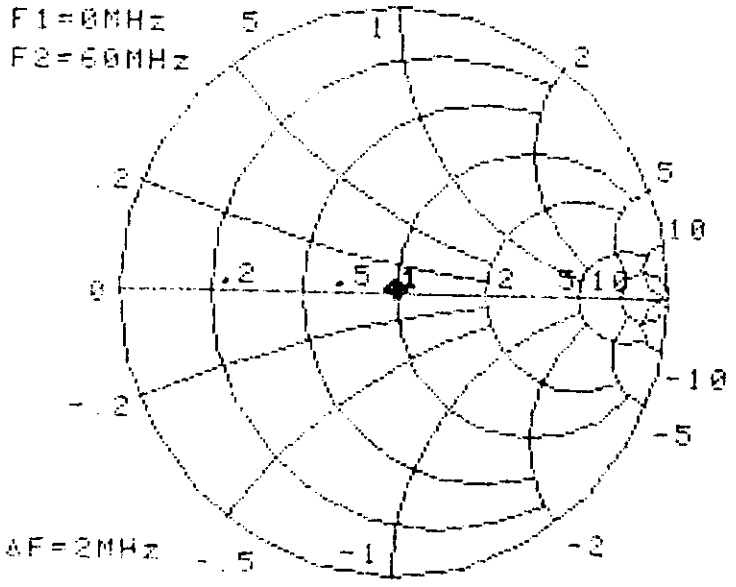

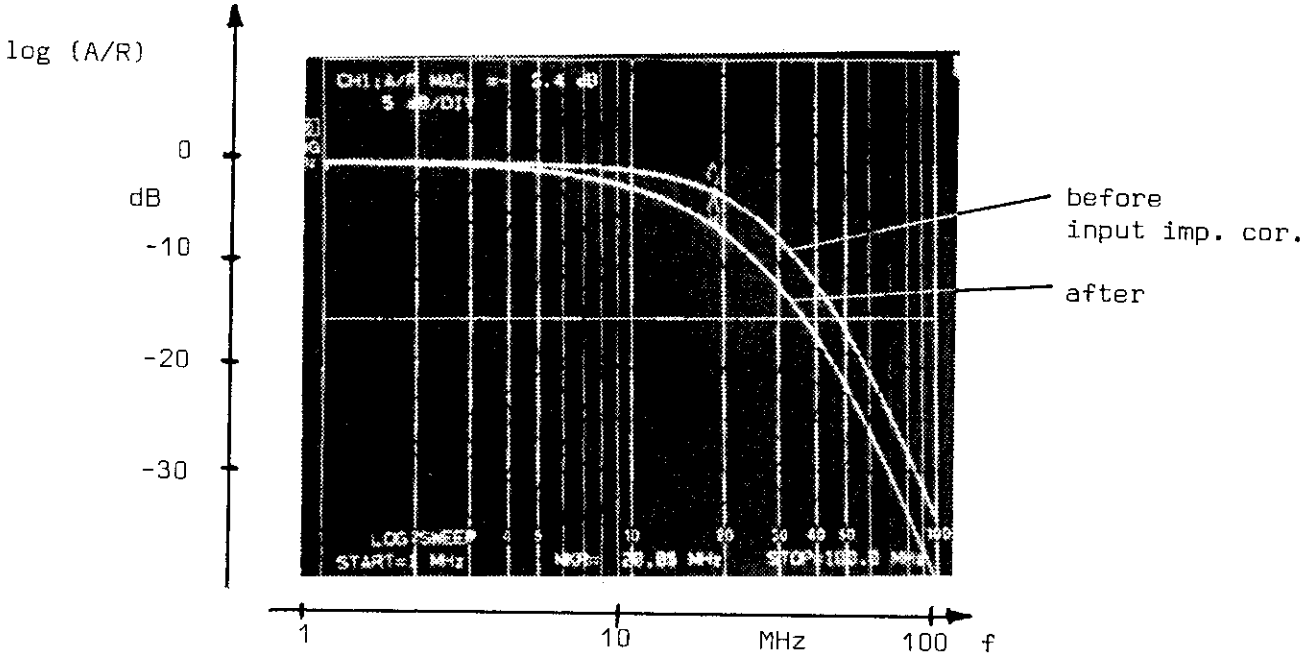

Fig. 6.7 Correction of the input impedance of the filter shown in Fig. 6.6 with a capacity C_c = 280 pF and a resistor R_c = 50Ω. the Smith chart becomes a point at 50Ω. The photo shows the frequency response (ratio between output A and input R) of the filter with and without correction.

4.2.83

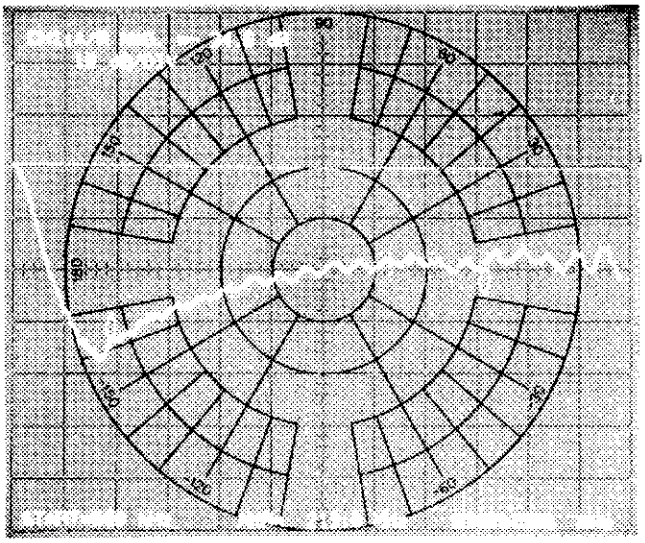

0.5 to 1300 MHz

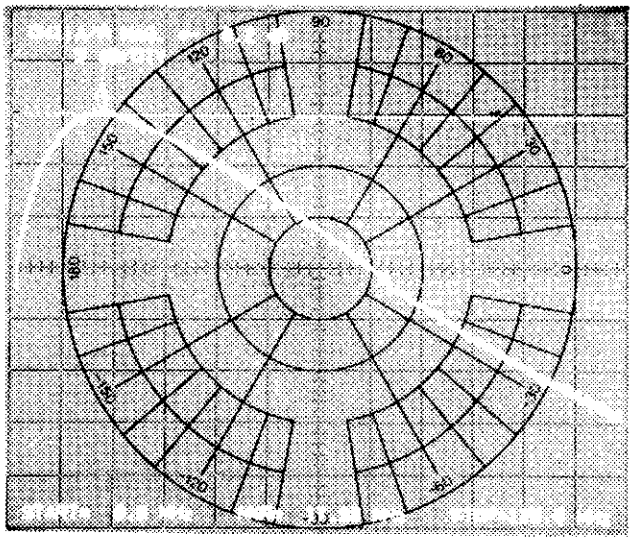

0 to 120 MHz

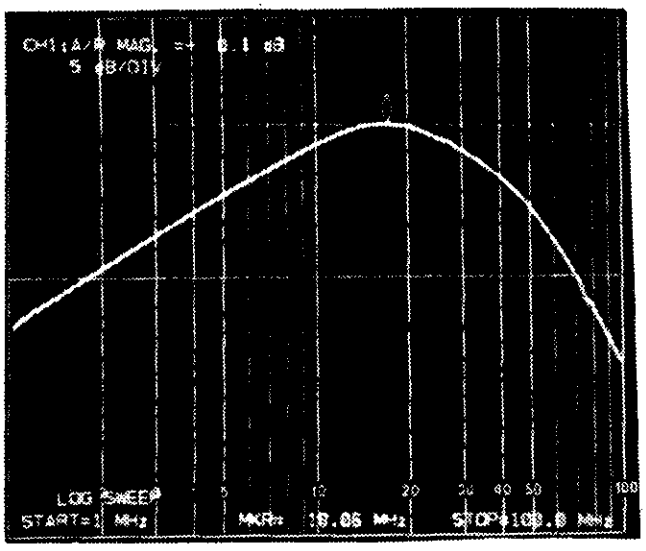

1 to 100 MHz (log)

Fig. 6.8 Response of a button with 20 MHz low-pass filter.

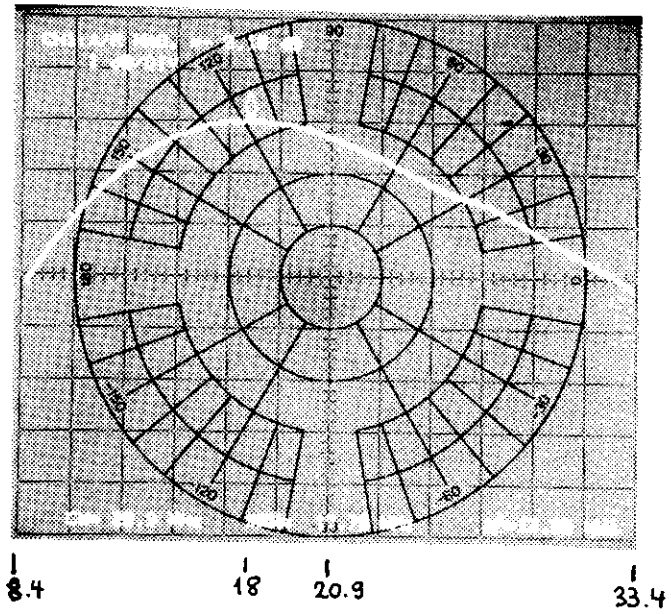

button and filter around the frequency f_m = 18 MHz of maximum response.

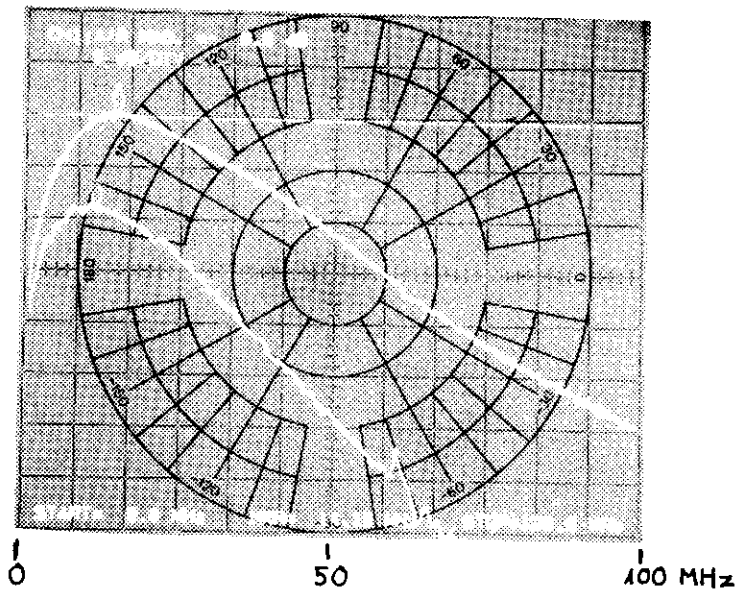

response of the button and filter with and without a simulated 750 m long CK50 cable.

Fig. 6.9 Frequency response of a button and low-pass filter with and without the simulated attenuation in a 750 m long CK50 cable.

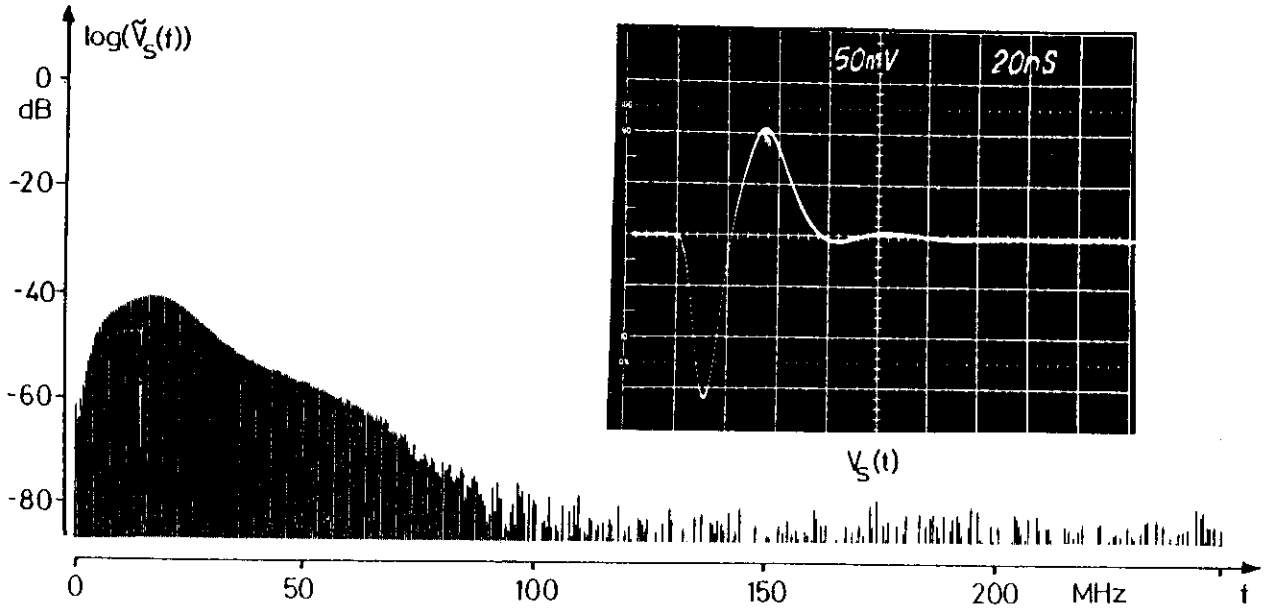

Fig. 6.10 Response of a button with low-pass filter having f_1 = 20 MHz, in time and frequency domain $V_s(t)$, $\tilde{V}_s(f)$ to a short pulse (see top of Fig. 3.14) from the generator which simulates the beam.

f_1 MHz	$\sqrt{2}\,\hat{V}_s$ mV	t_r n_s
10	0.13	35
20	0.51	17.5
50	3.20	7
100	12.83	3.5

Table 6.3. Signal amplitudes and pulse length just after the low-pass filter as a function of the filter cut-off frequency f_1 for injection condition with $N_b = 2.2 \cdot 10^9$ particles/bunch and button parameters $Z_\infty = 0.3\Omega$ $C_e = 15$ pF.

For a finite cable length the signal is slightly changed since the cable attenuation depends on frequency; fig. 5.3.

A more detailed calculation gives the resultant central frequency f_p, band width $\pm\Delta f$ and pulse length observed at the end of 750 m of CK50 cable.

The noise of the wide-band amplifier has been taken into account by taking the basic rms noise $V_n = \sqrt{4kTR_o 2\Delta F}$, a 6 dB noise figure for the amplifier and the proper attenuation of the noise by the cable having an effective band width of $2\Delta F \approx 25$ MHz. The results are listed in table 6.4 where the final signal to noise ratio of the final sum signal is also shown and the corresponding position resolution Δx. For the case of f_l = 20 MHz, the results have been verified in the laboratory test.

f_l	cable atten.	f_p	$\pm\Delta f$	t_r	$\hat{V}_d$	$\hat{V}_{ns}$	$\frac{2\hat{V}_d}{\sqrt{2}\,\hat{V}_{ns}}$	Δx
MHz	dB	MHz	MHz	ns	mV	µV		mm
10	6	7	6.5	41	0.09	27	4.7	7.6
20	9	12.5	12	25	0.26	27	13.6	2.6
50	13.5	22.5	20.5	12	1.15	27	60.2	0.6
100	21	33	31.5	9	1.93	27	101.1	0.35

Table 6.4 Parameters of the complete wide band system for injection condition with $2.2 \cdot 10^9$ particles/bunch ($3.5 \cdot 10^{-10}$As) as a function of the low-pass filter cut-off frequency f_l. The cable attenuation corresponds to 750 m of CK50 cable, f_p, Δf and t_r are the resulting centre frequencies, bandwidth and pulse length respectively, V_d is the peak signal from two buttons, $\hat{V}_{ns}$ the final noise voltage and Δx the resulting position resolution for a signal-to-noise ratio of unity.

6.2.5 Wide-band signal processing resolution

For f_l = 100 MHz the system resolution limited by the front-end noise is $\Delta x \approx 0.35$ mm as shown in Table 6.4. This represents the uncertainty of the position measurement on the first injected turn with $2.2 \cdot 10^9$ particles in the single bunch due to the internal noise without taking any external noise into account. If the beam circulates the effect of the amplifier noise can be reduced by averaging over several revolutions. To give an example an average

of ten turns would increase the signal to noise ratio by $\sqrt{10}$ and bring us close to the desired resolution of $\Delta x \approx 0.1$ mm.

This result shows that the minimum number of charges per bunch, $2.2 \cdot 10^9$, is a bare minimum to reach the desired resolution for the system prior to accumulation.

The low level of signal, 1.9 mV with the best solution at $f_0 = 100$ MHz, with no active part next to the chamber, will still require an amplifier in the tunnel with a gain of about 30 to 60 dB for the transmitted pulse to be above the possible picked-off parasitic noise. The amplifier will have to be switchable in order not to be damaged at the highest beam intensities, which may reach a factor from 200 to 1,200 times above injection level.

The next step prior to digital conversion could be a peak and hold circuit[41] or integrate and hold and a beam signal auto-trigger for the acquisition sequence for both e^+e^- signals. Such circuits are under development and are feasible.

7. System test by beam simulation in the tunnel

It is very important to run in the system prior to the first injection and during operation to maintain its calibration. This is feasible by the production of a test pulse of high stability and equal amplitude on the two channels for the wide-band approach.

This test pulse can be of much smaller amplitude and larger duration than that of the beam. It should be introduced at the input of the filter in order to test the total analog transmission chain. Since the voltage level is independent of C_e, there is no need to inject the signal on the electrode, if the coupling to the beam is mechanically well-defined and stable in time. The test signal can be distributed from each alcove by two 750 m cables and passive pick-off circuits. There are still timing sequences to be checked in accordance with the timing of the acquisition system and the propagation delays.

8. Acquisition system

A simultaneous acquisition of all the LEP PU's has many advantages. With the same hardware and only by software commands, one can obtain:

- an exact picture of the closed orbit (c.o.) at a given time
- first turn trajectory
- betatron oscillations
- betatron phase advance between PU's and β values.

A sequential multiplexer would have reduced possibilities and reliability.

It is not foreseen at present to make simultaneously the acquisition of the four e^+ and the four e^- LEP bunches. Only one bunch of a given sign will be acquired at a time. The type of particles and the bunch number can be selected before any closed orbit measurement.

The proposed system could give five different c.o. corresponding to five programmable timing values within one LEP cycle, two c.o. acquisitions being separated by at least 0.2 s.

The beam position acquisition software must fulfil two special requirements:

- the data base should be centralised in an accessible place (e.g.: local computer in each auxiliary building or in the accessible intersection cave
- the local microprocessors (μP) directly connected to the hardware should contain a very simple Data Module Subroutine (DMS), only hardware oriented, to facilitate its use by maintenance teams mainly interested in raw data. Moreover, since two out of three of these μPs are located in the alcoves, it is better for reasons of reliability to limit their hardware and software to a bare minimum[41].

These requirements can be met by adopting a two level DMS philosophy. One simple DMS (DMS 1) will reside in the μP. Whether the acquisition is made from individual 64-word buffer memories or by direct transfer after each LEP revolution to a RAM depends on the available technology. A μP dealing with a maximum of 16 PU's (one plane at the alcove level) seems compatible with direct acquisition. The DMS 1 properties will be such as to give back the raw data for first turn trajectory, closed orbit (by averaging over 40 turns) and betatron oscillations and to receive orders setting the gain and the system mode of real-time operation.

The other DMS (DMS 2) will be located in the beam monitoring process assembly along with its data base. It will have no real-time tasks. The properties will be more "operation" oriented, but still of firmware nature.

The DMS 2 will give back the processed first turn and average central orbit (position in mm) and the difference between them, their mean value and standard deviation upon request. It could also compute the phase advance between two PUs and the corresponding averaged β value. It will set the acquisition timing sequences (independently of the low level μPs) and the real-time operation mode of the μPs (see Chapter 9).

The data transfer between each alcove μP and the BM processor will be of the order of 64 words of two bytes per orbit acquisition (two data x 32 monitors). Between the BM processor and the MCR the traffic will be 90 words (position in mm) per orbit acquisition, i.e. 90 single-plane monitors.

If both first turn and first average orbit are acquired at the same injection, the data transfer could be doubled.

The β-measurement results will be given in two words, one for the magnitude and one for the phase, for 45 vertical and 45 horizontal monitors. The β function could be given either in difference between two successive monitors or in absolute value relative to the injection point or some other fixed reference point.

One of the advantages of this scheme is to maintain the same access protocol (i.e. DMS) down to the last intelligent piece of hardware. It will allow any easy and straightforward access to low level μP's, even from the MCR, for test or maintenance programs. Locally the technicians can test their hardware quite easily (including the μP) by disconnecting the link to the central control system and connecting it to a standard stand-alone system.

The system design, in its firmware form, would be eased if the LEP control network accepts interrupts from the low-level processors.

Sketches of how this philosophy could be implemented are given in Figures 8.1 and 8.2.

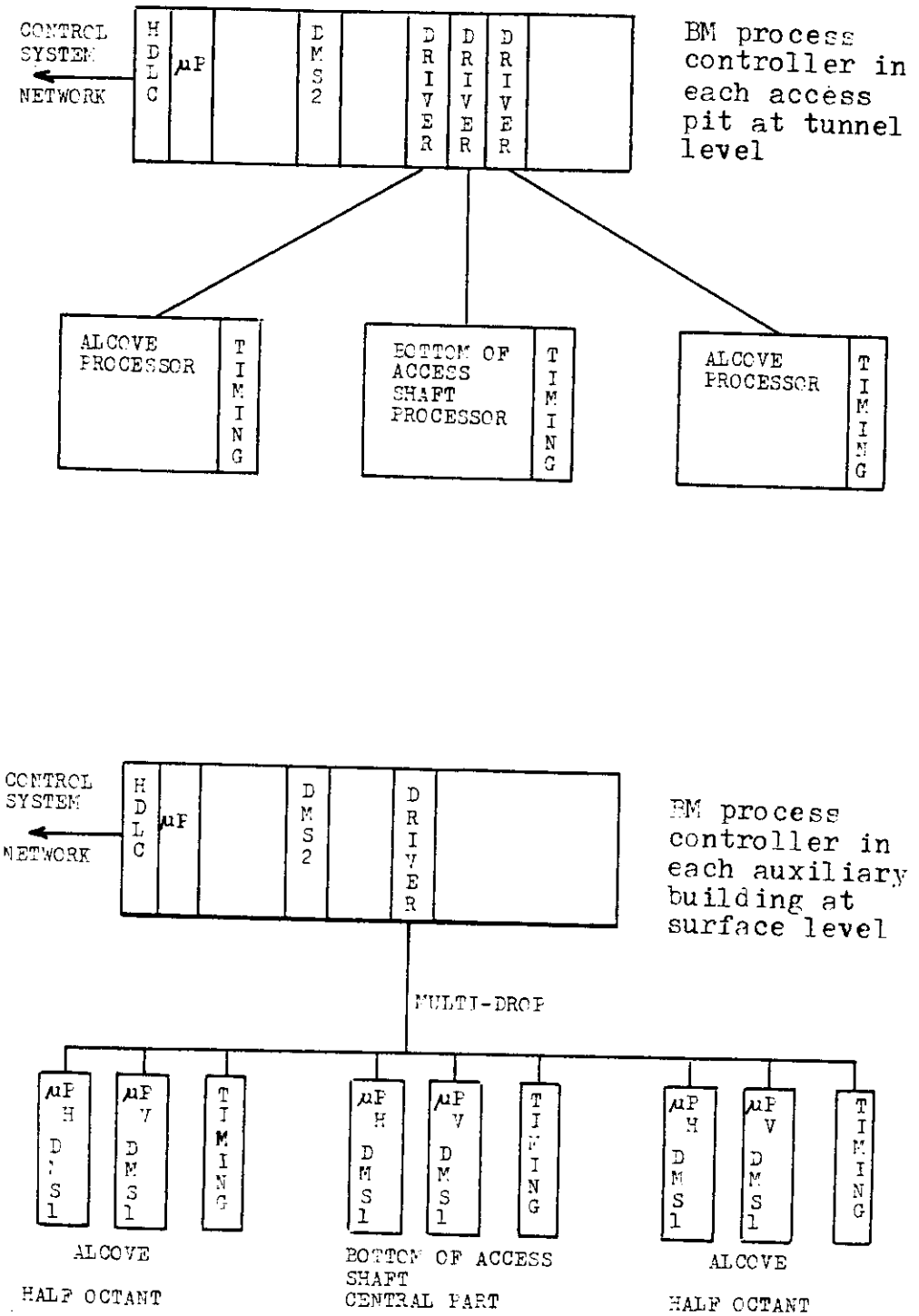

Fig. 8.1 Two possible layouts for the acquisition system.

Another advantage of the multi µP system resides in the fact that the µP can do surveillance tasks at the background level: hardware surveillance by the low-level µPs and closed orbit surveillance by the BM processor.

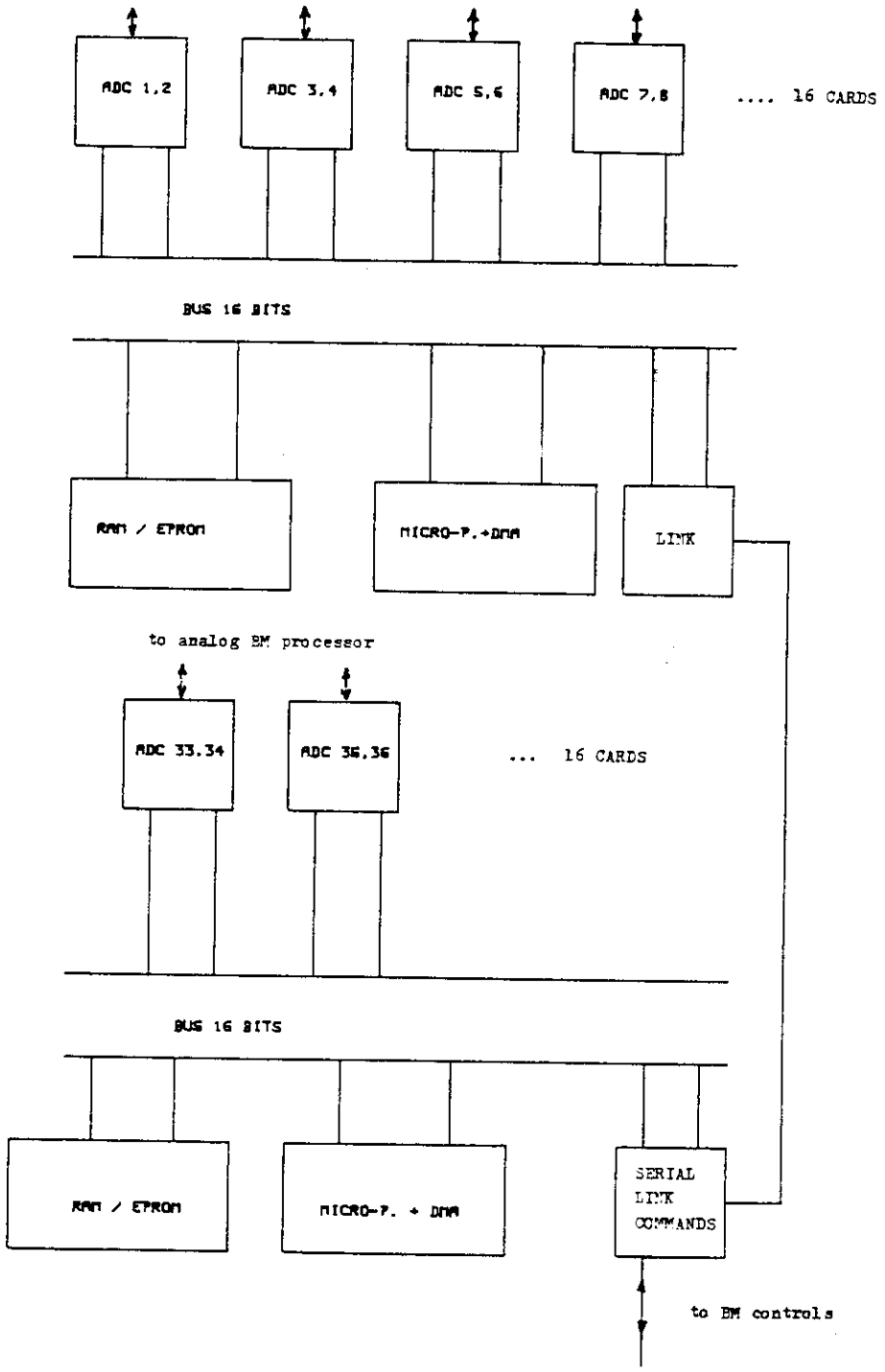

Fig. 8.2 Proposed structure of the alcove processor.

9. Measurement of the lattice functions[47]

9.1 Introduction

The beam position measurement system can also be used to measure the beta function and the dispersion around the ring. The proposed method relies on exciting a betatron or phase oscillation and measuring its amplitude and phase with the beam position monitors. This requires a read-out system fast enough to follow such oscillation and a memory large enough to store these measurements obtained for the duration of many oscillations. In the interaction regions, the proposed methods are not sufficiently accurate and special measurements will be performed there.

9.2 Direct measurement of the relative β-functions

A continuous betatron oscillation having an amplitude A ≈ 4 mm at the average value of the beta function of~90 m is excited. The amplitude of this oscillation can be measured at each position monitor with a precision of A ≈ 0.2 mm. The observed amplitude A(s) is proportional to $\sqrt{\beta(s)}$ and therefore:

$$\frac{\Delta\beta}{\beta} \approx 2\,\frac{\Delta A}{A}$$

This allows the relative value of the beta function to be measured with an accuracy of ~8% at the quadrupoles which focus in the direction of the excited oscillation.

9.3 Measurement of the betatron phase advance

In this case the phase of the excited betatron oscillation is measured at two position monitors and compared. From this the betatron phase advance $\mu_2-\mu_1$ between the locations of the monitors can be obtained. By measuring this phase for the upper (n_+Q) and lower (n_-Q) betatron side band, most of the errors due to cable length can be suppressed. The measurement does not depend on the monitor calibration and is therefore quite precise. Experiments done in the ISR[45,46] indicate that the accuracy of this phase measurement is about $\Delta\mu \approx 5^{\circ} = 87$ mrad. The phase measurement does not give

the beta function directly but the integral over its reciprocal value and can be compared with the calculated value for the ideal lattice. In particular the phase advance from one interaction point to the next might be of interest. Another application is the location of the quadrupole error $\Delta(K\ell)$. Such an error produces a wiggle of the beta function around the ring with a period length being half the betatron wave length. The phase advance between two points which are nominally $\mu_2-\mu_1 = n\pi$ apart, is not changed by the quadrupole error unless it occurs between the two points. In the latter case it gives a phase error:

$$\Delta\mu = \frac{\beta\Delta(K\ell)}{2}$$

Using the short lens approximation for a FODO lattice with a phase advance μ_c per cell and lenses with focusing strengths $\pm K\ell$, we obtain for the beta function at the lenses:

$$\beta_{max/min} = \frac{2}{K\ell\ \cos(\mu_c/2)}\left(1 \pm \sin(\mu_c/2)\right)$$

The relation between the focusing error $\Delta(K\ell)$ and the resulting change μ in the phase advance is therefore:

$$\frac{\Delta(K\ell)}{K\ell} = \frac{\cos\ (\mu_c/2)}{1 \pm \sin(\mu_c/2)}\,\Delta\mu$$

The resolution for the measurement of a single quadrupole error obtained by observing the phase advance with an accuracy of 5^o is listed in table 9.1.

μ_c	$\frac{\Delta(K\ell)}{K\ell}$
60^o	5%
90^o	3.6%

Table 9.1 Resolution for the measurement of a quadrupole error using a phase observation with 5^o resolution.

If the quadrupole error is due to a horizontal displacement of the sextupole this phase measurement could determine this orbit error in the 60° lattice with a resolution of $\Delta x \approx 22$ mm in the F sextupole and $\Delta X \approx 7$ mm in the D sextupole. The resolution of these measurements is not very good but could be useful to locate something which is grossly wrong. It would be nice to improve the accuracy of the measurement.

9.4 Dispersion measurement

We assume an excited phase oscillation with an amplitude $A \sim 4$ mm at an average dispersion $D \sim 1.8$ m which corresponds to $\Delta p/p \sim 2.2 \cdot 10^{-3}$. This amplitude is measured at the position monitors with a precision of $\Delta A \sim 0.2$ mm which gives a dispersion measurement with an accuracy :

$$D = \frac{\Delta A}{\Delta p/p} \approx 0.1 \text{ m}$$

for both planes. A phase measurement would not be accurate enough to give any useful information since the phase advance of the phase oscillation is only about 36° per revolution.

Acknowledgements

We thank G. Corazza, C. Hauviller and R. Perin for helping us to solve the mechanical problems. We would also like to thank the LEP Vacuum Group, especially J.-C. Brunet, J.-C. Godot, O. Gröbner and T. Wikberg, for their help with the vacuum problems and with the arrangement of the monitors with respect to the other equipment. We have profited from many discussions with P. Lebrun and H. Isch related to the possibilities of orbit corrections. Thanks are also due to Y. Marti for computing the effect of magnetic errors and for simulating correction schemes and to H. Henke for his collaboration with the test bench measurements.

References

1) M. Placidi: "Extended Parameter List for LEP Version 12 Phase 1", LEP Note 394 (1982).

2) Y. Baconnier, B. de Raad, K. Hübner, J.H.B. Madsen: "Mode of Operation for the LEP Injection System", LEP Note 395 (1982).

3) E. Keil: "Beam Crossings and Beam Separations in LEP-70", LEP Note 70/7 (1977).

4) D. Potaux: "Séparation des Faisceaux au Milieu des Arcs et Séparation Induite au Milieu des Sections d'Insertion dans LEP-7", LEP Note 70/7 (1977).

5) J. Jowett: "Beam Separation in Mid-Arc for Eight-Bunch Operation of LEP", LEP Note 368 (1982).

6) T. Weiland: "On the Quantitative Prediction of Bunch Lengthening in High Energy Electron Storage Rings", DESY 81-088 (1981).

7) D. Brandt: "Simulation of Longitudinal Single-Bunch Effects in LEP", CERN/ISR-TH/82-09 (1982).

8) D. Brandt: Private Communication (1982).

9) M. Bassetti: "Effects due to the Discontinuous Replacement of Radiated Energy in an Electron Storage Ring", Proc. of the 11th Int. Conf. on High Energy Accelerators, CERN, Geneva (1980) p. 650.

10) G. Guignard, Y. Marti: "Miscrossing due to Radiation Losses in LEP Version 11", LEP Note 340 (1981).

11) K. Steffen, J. Kewisch: "Study of Integer Difference Resonances in Distorted PETRA Optics", DESY-PET-76/09 (1976).

12) G. Guignard, Y. Marti: "PETROC* Users Guide (*PETROC is the CERN Version of the Program PETROS written at DESY)", CERN-ISR/BOM-TH/81-32 (1981).

13) G. Guignard, Y. Marti: "Numerical Simulation of Closed Orbit Corrections in LEP Version 11", LEP Note 335 (1981).

14) G. Guignard, Y. Marti: "Closed Orbit Corrections, Stability and Damping Behaviour in the Detuned LEP Version 11", LEP Note 355 (1982).

15) G. Guignard: "Closed Orbit Correction in LEP Version 11 with a Phase Advance of 60° per Cell", LEP Note 403 (1982).

16) Ph. LeBrun: "Preliminary Design of the Magnetic System for Orbit Correction in LEP", LEP Note 332 (1981).

17) H.D. Bremer, J. Kewisch, H.C. Lewin, H. Mais, R. Rossmanith, Rüdiger Schmidt, D.P. Barber: "Optimizing the Degree of Polarization in PETRA", DESY 82-026 (1982).

18) B.M. Montague: Private Communication (1982).

19) The LEP Study Group: "Design Study of a 15 to 100 GeV e^+e^- Colliding Beam Machine (LEP)", CERN/ISR-LEP/78-17, "Blue Book" (1978).

20) R. Bossart, A. Chapman-Hatchett, E. d'Amico, J.P. Papis, H. Rossi, V. Rossi: "Beam Position Measurement for Proton-Antiproton Operation in the SPS", Proc. of the 11th Int. Conf. on High Energy Accelerators, CERN, Geneva (1980) p. 486.

21) DESY, "PETRA, Updated Version of the PETRA Proposal", Feb. 1976.

22) J.-L. Pellegrin: "A Review of Accelerator Instrumentation", Proc. of the 11th Int. Conf. on High Energy Accelerators, CERN, Geneva (1980) p. 459.

23) T. Katsura, H. Nakagawa, S. Shibata: "Beam Diagnostics Instrumentation in the Photon Factory Storage Ring", IEEE Trans. on Nucl. Sci. NS-28 no. 3 2353 (1982).

24) J.-L. Pellegrin: Private Communication, office memo Aug. 1982.

25) Hajime Ishimaru: "Al-Alloy-Ceramic Ultrahigh Vacuum and Cryogenic Feedthrough Useful from DC to 6.5 GHz.", Vacuum, Vol. 32 753 (1982).

26) T. Yamamoto, H. Höfert: "Evaluation of the Peak Power of Pulsed Synchrotron Radiation from LEP", CERN-HS-RP/IR/81-58 (1958).

27) K. Burn: "Doses and Photo-Currents in the LEP Pick-Up Electrodes", Technical Memo CERN-HS-RP/TM/82-51 (1982).

28) P. Sievers: "Maximum Energy Deposition Densities and Doses Inside the LEP Vacuum Chamber", LEP Note 381 (1982).

29) J. Bredy, P. Lalande, A. Permuy: "Test de Composant pour CERN", CEA-DAM/LEP.3/D-3286 (1982).

30) J. Bosser, B. Bouchet, L. Burnod, J. Camas, G. Ferioli, H. Rossi: "Experiment at LURE (DCI-Orsay) held March 8/9, 1982", CERN-SPS/ABM/LB/Note 82-01 (1982).

31) R. Bossart, J. Bosser, B. Bouchet, L. Burnod, V. Rossi: "Experiment at DCI (Orsay) held June 26, 1982", CERN-SPS/ABM/LB/Note 82-08 (1982).

32) W. Unterlerchner, J. Delfosse, D. Jenson: "Recent Work on Bakable Flange Pairs of Dissimilar Metals", CERN-ISR-VA/80-14 (1980).

33) D. Boussard, L. Burnod: "Choix du type de détecteurs de position pour le SPS", CERN Lab II-CO/Bm/72-6 (1972).

34) T. Linnecar: "The High Frequency Longitudinal and Transverse Pick-Ups Used in the SPS", CERN-SPS/ARF/78-17 (1978).

35) N.N. Lebedev, I.P. Skalskaya, Y.S. Ufland: "Worked Problems in Applied Mathematics", Dover Publ. New York p. 205.

36) M. Sands, J. Rees: "A Bench Measurement of the Energy Loss of a Stored Beam to a Cavity", SLAC-PEP-95 (1974).

37) J. Peters: "Bench Measurements of the Energy Loss of a Stored Beam to Vacuum Components", DESY PET-77/14 (1977).

38) G. Cavallari, A. Giannelli, V. Picciarelli: "Time-Domain Measurement of the Loss Factor in a Quasi-Spherical Cavity for Superconducting LEP", CERN-EF/RF/82-2 (1982).

39) H. Hahn, F. Pedersen: "On Coaxial Wire Measurements of the Longitudinal Coupling Impedance", BNL 50870 (1978).

40) R. Bossart, J. Bosser, L. Burnod, A. Chapman-Hatchett, E. D'Amico, P. Mills: "The SPS Beam Instrumentation and Closed Orbit Correction", IEEE Trans. on Nucl. Sci., NS-24 no. 3 1733 (1977).

41) J. Borer, D. Cocq, H. Kropf, C. Paillard, P. Tranchant: "Système de Mesure de Trajectoires en TT6-TT1 et d'Orbites en R2 pour les Antiprotons aux ISR", Partie I, CERN/ISR-RF/82-08 (1982); Partie II, Note Technique, ISR-RF/JB/DC/CP/cb/TN6 (1982).

42) J. Bosser, L. Burnod, G. Ferioli: "Beam Position Measurements by Use of 90° Hybrids (Proposed for LEP)", CERN-SPS/ABM/83-01/00586 (1983).

43) D. Cocq: Internal Technical Note.

44) A.I. Zverev: "Handbook of Filter Synthesis", John Wiley and Sons Inc., New York - London - Sydney (1967).

45) J. Borer, A. Hofmann: "Measurement of Beta Function and Betatron Phase Advance by Means of the Beam Transfer Function", ISR Performance Report Run 950 (1982).

46) J. Borer, A. Hofmann, J-C. Juillard, T. Risselada: "Measurement of Betatron Phase Advance (2), ISR Performance Report Runs 1246 and 1250 (1982).

47) J. Borer, A. Hofmann, J-P. Koutchouk, T. Risselada and B. Zotter: "Measurement of Betatron Phase Advance and Beta Function in the ISR", 1983 Particle Acc. Conf., Santa Fe, and CERN/LEP-ISR/83-12.